X-RAY VARIABILITY CHARACTERISTICS OF THE SEYFERT 1 GALAXY NGC 3783

A. MARKOWITZ[1,2]

[1] X-RAY ASTROPHYSICS LABORATORY, CODE 662, NASA/GODDARD SPACE FLIGHT CENTER,
GREENBELT, MD 20771; agm@milkyway.gsfc.nasa.gov
[2] N.A.S./N.R.C. RESEARCH ASSOCIATE

ABSTRACT

We have characterized the energy-dependent X-ray variability properties of the Seyfert 1 galaxy NGC 3783 using archival *XMM-Newton* and *Rossi X-ray Timing Explorer* data. The high-frequency fluctuation power spectral density function (PSD) slope is consistent with flattening towards higher energies. Light curve cross correlation functions yield no significant lags, but peak coefficients generally decrease as energy separation of the bands increases on both short and long timescales. We have measured the coherence between various X-ray bands over the temporal frequency range of $6 \times 10^{-8} - 1 \times 10^{-4}$ Hz; this range includes the temporal frequency of the low-frequency power spectral density function (PSD) break tentatively detected by Markowitz et al. and includes the lowest temporal frequency over which coherence has been measured in any AGN to date. Coherence is generally near unity at these temporal frequencies, though it decreases slightly as energy separation of the bands increases. Temporal frequency-dependent phase lags are detected on short time scales; phase lags are consistent with increasing as energy separation increases or as temporal frequency decreases. All of these results are similar to those obtained previously for several Seyfert galaxies and stellar-mass black hole systems. Qualitatively, these results are consistent with the variability models of Kotov et al. and Lyubarskii, wherein the X-ray variability is due to inwardly propagating variations in the local mass accretion rate.

Subject headings: galaxies: active — galaxies: Seyfert — galaxies: individual (NGC 3783)

1. INTRODUCTION

Seyfert active galactic nuclei (AGNs) and stellar-mass black hole X-ray binary systems (XRBs) both exhibit rapid, aperiodic X-ray variability that likely originates in the innermost regions of these compact accreting objects. The dominant radiation at hard X-rays is generally thought to be inverse Comptonization of soft seed photons by a hot corona (e.g., Shapiro, Lightman & Eardley 1976, Sunyaev & Titarchuk 1980), though the exact geometry is uncertain and numerous models have been invoked (e.g., Zdziarski et al. 2003). Possible configurations include, but are not limited to, a neutral accretion disk sandwiched by a patchy, and possibly outflowing, corona (e.g., Stern et al. 1995, Svensson 1996, Beloborodov 1999), as well as a hot inner disk radially surrounded by a cold disk, with a variable transition radius (e.g., Zdziarski, Lubinski & Smith 1999).

The X-ray variability can be characterized by fluctuation power spectral density functions (PSDs) which show the "red-noise" nature of the variability at relatively high temporal frequencies in both AGNs and XRBs. In XRBs, the X-ray variability characteristics and PSD shape are known to correlate with energy spectral state. Modeling of the broadband PSDs of XRBs usually utilizes some combination of one, two, or more Lorenztians, which tend to dominate in the so-called low/hard energy spectral state, plus a broadband noise component characterized as $P \propto f^{-1}$, which tends to dominates in the high/soft state (e.g., in Cyg X-1; see Axelsson et al. 2005, Belloni et al. 2005). The peak frequency of the Lorentzians tend to move towards relatively higher temporal frequencies as luminosity and accretion rate increase in many transient sources

(e.g., van der Klis 2004, Kalemci et al. 2004, Rodriguez et al. 2004). The (relatively more stable) black hole candidate Cyg X-1 tends to spend a majority of its time in the low/hard state, wherein the PSD is dominated by two Lorentzians that typically peak near 0.1–0.3 and 3–10 Hz (e.g., Nowak et al. 1999a,b). The PSD of the high/soft state of Cyg X-1 is dominated by $1/f$ broadband noise at the lowest temporal frequencies, with a high-frequency break usually found near 10 Hz. Global accretion rate is the likely driver in determining whether an XRB appears in the low/hard or high/soft state, with the transition usually occurring at $\sim 2\%$ of Eddington (Maccarone 2003). Quasi-periodic oscillations (QPOs) are routinely seen in XRB PSDs. They are generally divided into two broad classes, low- and high-frequency QPOs, which usually appear in the ranges $\sim 0.05 - 30$ Hz and $\gtrsim 100$ Hz, respectively.

Broadband X-ray PSDs have also been constructed for AGNs, allowing modeling of the overall PSD shape and also showing the red-noise variability at high frequencies. However, the quality of the data precludes complex modeling of the PSD shape; for example, the QPOs routinely seen in XRBs, even if they existed in AGN, could not likely be detected with currently available AGN data (Vaughan & Uttley 2005). However, modeling AGN PSDs with broken power-law models has successfully yielded breaks on time scales of a few days or less (Uttley, McHardy & Papadakis 2002; Markowitz et al. 2003b [hereafter M03]; Marshall et al. 2004; McHardy et al. 2004), with PSD power-law slopes $\sim$−2 above a break and $\sim$−1 below it. The similarity in Seyferts' and XRBs' broadband PSD shapes and the suggested possible scaling of the PSD break time scale with black hole mass (e.g., M03, McHardy et al. 2004)

1

support the suggestion of similar X-ray variability mechanisms being present in both classes of accreting compact objects. The picture emerging is one in which Seyferts and XRBs are scaled versions of each other in black hole mass and X-ray variability time scale, though it is not yet clear if Seyferts are direct analogues of XRBs in the low/hard or high/soft state (see e.g., McHardy et al. 2004, Markowitz & Uttley 2005). An additional link between Seyferts and XRBs arises in the linear relation between flux and absolute rms variability (e.g., Uttley & McHardy 2001, Edelson et al. 2002) that exists in both AGN and XRBs.

The observed cross-spectral properties, namely the coherence function (Vaughan & Nowak 1997) and phase lags, are also similar in both object classes, further supporting this notion. The coherence is generally seen to be unity over a wide range of temporal frequencies in both AGNs and XRBs, though with a deviation from unity above the high-frequency PSD break frequency (e.g., Nowak et al. 1999a, 1999b; Papadakis, Nandra & Kazanas 2001, Vaughan, Fabian & Nandra 2003b [hereafter VFN03], McHardy et al. 2004). Relatively harder X-rays are seen to generally lag those at softer X-ray energies, with the lag between bands increasing with increasing energy separation; this is consistent with a basic prediction of the Comptonization hypothesis. However, the lags are also observed to depend on temporal frequency: more slowly varying components show a relatively longer time lag (e.g., Miyamoto & Kitamoto 1989, Miyamoto et al. 1991, Nowak et al. 1999a in XRBs; Papadakis, Nandra & Kazanas 2001, VFN03, Vaughan & Fabian 2003, McHardy et al. 2004 in Seyferts). Additionally, the slope of the PSD above the high-frequency break is observed to flatten as energy increases (e.g., Nowak et al. 1999a, Lin et al. 2000 in XRBs; Nandra & Papadakis 2001, VFN03, McHardy et al. 2004 in Seyferts). For instance, using Fourier-resolved spectroscopy, Papadakis, Kazanas & Akylas (2005) found that, above 2 keV, the ratio of hard X-ray variability to soft X-ray variability increased towards relatively higher temporal frequencies. Similarly, Leighly (2004) also found the structure function of the narrow line Seyfert 1 galaxy 1H 0707–495 to flatten towards higher photon energies on time scales $\lesssim 3$ ksec.

In this paper, we investigate the relationship between flux variations in different energy bands in the Seyfert 1 galaxy NGC 3783. M03 established the presence of a break in this object's 2–10 keV PSD at 4×10^{-6} Hz. In addition, M03 found tentative evidence for a second, low-frequency break near 2×10^{-7} Hz, below which the PSD power-law slope flattens to 0. This makes NGC 3783 one of only two Seyfert galaxies (along with Ark 564; M03) known so far in which dominance of a f^{-1} power-law component at the lowest temporal frequencies can be ruled out. M03 did not explore the energy dependence of the PSD slope above the break. In this work, we study the cross-spectral properties and energy-dependence of the high-frequency PSD of NGC 3783 using data obtained from an *XMM-Newton* long-look and from regular monitoring by the *Rossi X-ray Timing Explorer* (*RXTE*). §2 describes the *XMM-Newton* and *RXTE* light curve extraction. Softness ratios, high-frequency PSD measurement, cross- and auto-correlation functions, and cross-spectral analysis are presented in §3. §4 compares these results to previous findings for AGN

and XRBs and discusses these results in the context of Comptonization models and X-ray variability mechanism models.

2. OBSERVATIONS AND DATA REDUCTION

2.1. *XMM-Newton Data Reduction*

NGC 3783 was observed by *XMM-Newton* on 2001 Dec. 17–21, over two full satellite orbits, revolutions 371 and 372. This sampling is hereafter referred to as short-term sampling. This paper uses data taken with the European Photon Imaging Camera (EPIC), which consists of one pn CCD back-illuminated array sensitive to 0.15–15 keV photons (Struder et al. 2001), and two MOS CCD front-illuminated arrays sensitive to 0.15-12 keV photons (MOS1 and MOS2, Turner et al. 2001). Data from the pn were taken in Small Window Mode; data from the MOS detectors were taken in Full Window Mode. This paper will concentrate primarily on data obtained with the pn, though MOS2 data were also analyzed for consistency. Data from the MOS1 were taken in Fast Uncompressed mode and are not used here. The medium filter was used for all detectors. Light curves were extracted using XMM-SAS version 6.0 using standard extraction procedures. Data were selected using event patterns 0–4 for the pn and 0–12 for the MOS2. Hot, flickering, or bad pixels were excluded. Source light curves were extracted from a circular region of radius 40″; background light curves were extracted from circles of identical size, centered ~3′ away from the core. Due to increased background levels at the end of each satellite orbit, the final 7 ksec and 13 ksec were excluded from the ends of revolutions 371 and 372, respectively. This reduction yielded two pn light curves of 129.9 ksec (rev. 371) and 123.8 ksec (rev. 372) in duration, separated by a 42.4 ks gap. The MOS2 light curves were 130.5 ksec (rev. 371) and 121.2 (rev. 372) in duration, separated by a 41.7 ksec gap. The revolution 371 light curves were uninterrupted except for gaps of 4.8 ksec (pn) and 5.0 ksec (MOS2) that occurred about 57 ksec after the start of the observation. The revolution 372 light curves were uninterrupted. Data were extracted over the 0.2–12 keV (total), 0.2–0.7 keV (soft), 0.7–2 keV (medium), and 2–12 keV (hard) bandpasses (also referred to as T, S, M and H bands, respectively, below). The hard bandpass was further subdivided into the 2–4, 4–7, and 7–12 keV bandpasses (hereafter referred to as the H1, H2, and H3 bands, respectively) for purposes of calculating the coherence function below. The 0.2–12 keV pn light curves for each revolution, binned to 1200 sec, are shown in Figure 1. Mean count rates for all of the pn light curves are listed in Table 1. Count rates and signal-to-noise values for the MOS2 light curves are not listed, but are usually ~1/2 of the corresponding pn light curve values.

2.2. *RXTE Data Reduction*

NGC 3783 was monitored by *RXTE* once every 4.3 d from 1999 Jan. 02 – 2002 Feb. 06 (hereafter referred to as long-term sampling) and once every other orbit (3.2 hr) from 2001 Feb. 20 – 2001 Mar. 12 (medium-term sampling); see M03 for observing details. Data were taken using *RXTE*'s proportional counter array (PCA; Swank 1998), which consists of five identical collimated proportional counter units (PCUs). For simplicity, data were

collected only from those PCUs which did not suffer from repeated breakdown during on-source time (PCUs 0 and 2 before 2000 May 12; PCU 2 only after 2000 May 12). Count rates quoted in this paper have been normalized to 1 PCU. Only PCA STANDARD-2 data were considered. The data were reduced using standard extraction methods and FTOOLS v5.3.1 software. Data were rejected if they were gathered less than $10°$ from the Earth's limb, if they were obtained within 30 min after the satellite's passage through the South Atlantic Anomaly, if ELECTRON0 > 0.1 (ELECTRON2 after 2000 May 12), or if the satellite's pointing offset was greater than $0°.02$.

As the PCA has no simultaneous background monitoring capability, background data were estimated by using PCABACKEST v3.0 to generate model files based on the particle-induced background, SAA activity, and the diffuse X-ray background. The 'L7-240' background models appropriate for faint sources were used. This background subtraction is the dominant source of systematic error in *RXTE* AGN monitoring data (e.g., Edelson & Nandra 1999). Counts were extracted only from the topmost PCU layer to maximize the signal-to-noise ratio. Light curves were generated over the 2–18 keV, 2–4 keV, 4–7 keV, 7–12 keV, and 12–18 keV bandpasses (the latter four are hereafter referred to as the H1, H2, H3 and H4 bands, respectively). The medium-term light curves were binned to 22.9 ksec to increase the variability to noise ratio; the long-term light curves were binned to 4.3 days. Standard errors were derived from the data in each orbital bin. The 2–18 keV *RXTE* light curves are shown in Figure 1. Mean count rates for all light curves are listed in Table 1.

3. ANALYSIS

The variability analysis presented in this paper consisted of several tests. Because the quality of the data and the variability-to-noise ratio were different for all three sampling patterns, and because the *RXTE* and *XMM-Newton* bandpasses only overlap at 2–12 keV, not all light curves could be used for each timing measurement.

Analyses using the short-term data concentrated primarily on the *XMM-Newton* pn light curves. The MOS2 data were of lower signal-to-noise; they were also analyzed, yielding results consistent with the pn data, and they are not discussed in detail here. Because gaps such as the one between the rev. 371 and rev. 372 *XMM-Newton* light curves complicate timing analysis, the two light curves from each revolution were treated separately in the analyses below (as opposed to combining the two light curves and interpolating across the large gap). The predicted level of variability power due to Poisson noise was calculated as $P_{Psn} = 2(\mu + B)/ \mu^2$, where μ and B are the net source and background count rates, respectively, and is listed in Table 1 for each light curve. For non-continuously observed data such as the *RXTE* data here, P_{Psn} is multiplied by the ratio of the mean sampling time to the duration of each individual visit, e.g., 22.9 for the medium-term data binned to 22.9 ksec and 368.64 for the long-term data binned to 4.3 days. The power due to Poisson noise in the MOS2 data is not listed, but is typically higher by a factor of ∼3 compared to the pn data.

Short-term variability amplitudes are presented in §3.1; variability amplitudes for the long and medium time scale

data have been discussed previously in M03 and Markowitz & Edelson (2004). Softness ratio (SR) light curves are presented in §3.2. The energy dependence of the high frequency PSD of NGC 3783 is presented in §3.3, using the short-term data. Cross correlation functions are presented in §3.4 for all three time scales. The cross-spectral properties, including the interband coherence properties and temporal frequency-dependent phase lags, are discussed in §3.5.

3.1. *Variability Amplitudes*

The *XMM-Newton* light curves were rebinned to the approximate time scale at which the Poisson noise begins to dominate over the intrinsic red-noise variability. This ensured that the fractional variability amplitude was quantified over temporal frequencies where the intrinsic red-noise variability is greater than the variability due to Poisson noise. This time scale was about 1200 s for the pn and 1600 s for the MOS2. Fractional variability amplitudes F_{var} and uncertainties were calculated using the formulation of e.g., Vaughan et al. (2003a) and are listed in Table 1 for all time scales and bandpasses. For the short-term data, only the pn results are listed; the MOS2 data yielded virtually identical results, though uncertainties on F_{var} were usually a factor of ∼2–3 higher compared to the pn data. For all data and time scales, F_{var} tends to decrease towards higher energies, consistent with numerous previous results (e.g., Markowitz & Edelson 2004 and references therein). The 2–12 keV short-term F_{var} values are quite similar to those measured over similar time scales by M03 for 2–10 keV *Chandra* light curves.

3.2. *Spectral Variability*

To explore spectral variability, softness ratio (SR) light curves were calculated for all time scales. The S/M, S/H and M/H ratio light curves were calculated for the short-term *XMM-Newton* data binned to 1200 s, and are overplotted on the corresponding sum of the two sub-band light curves (e.g., S-band + M-band) in Figure 2. The ratios of H1/H2, H1/H3, and H1/H4 for the long-term and medium-term *RXTE* data are also overplotted against their summed light curves in Figure 2; the ratios of H2/H3, H2/H4, and H3/H4 were calculated for completeness but are not shown in Figure 2. In these plots, all SR light curves (solid lines) and summed light curves (filled circles) have been mean-subtracted and normalized by the standard deviation to allow us to directly visually compare variations in flux or softness ratio. In general, the SR tracks the overall flux, consistent with numerous previous observations (e.g., Papadakis et al. 2002), but there are tentative indications in the short-term plots for spectral softening to precede increases in the summed flux by very roughly 5–10 ksec. In §3.4, we quantify this lag using cross-correlation functions; subsequent Monte Carlo simulations that quantify the significance of this claim show that it is preliminary at best. On medium and long time scales, there is no obvious lag.

3.3. *PSD energy dependence*

Previous studies (e.g., Nowak et al. 1999a, VFN03, McHardy et al. 2004) indicate that in Seyferts and XRBs, the modeled PSD high-frequency slope generally flattens

as energy increases, though break frequency generally does not depend on photon energy. The amplitude of the PSD at the break frequency generally decreases as photon energy increases, leading to light curve variability amplitudes which generally decrease as photon energy increases. The high-frequency PSD break for NGC 3783 measured by M03, 4×10^{-6} Hz, falls in the temporal frequency range covered by the medium-term *RXTE* data. However, as *RXTE* cannot detect <2 keV photons, the present *RXTE* data are not adequate to test these notions over a sufficiently wide energy range. Here, we assume a constant PSD break frequency of 4×10^{-6} Hz for all photon energies, and instead concentrate on the relative slopes of the high-frequency PSD at soft, medium, and hard energies using only the *XMM-Newton* pn data. PSDs derived from the MOS2 data are not presented here; the lower count rates and higher levels of power due to Poisson noise mean the MOS2 is of much lower quality, but the MOS2 results were generally consistent with those obtained using the pn data.

Power spectra for the soft, medium, and hard bandpasses were constructed in a manner similar to Uttley, M\(^c\)Hardy & Papadakis (2002), M03 and VFN03. The revolution 371 light curves were linearly interpolated across missing data points (the percentage of missing data was small, 4%; no data was missing for revolution 372). Each light curve's mean was subtracted. The power spectra were constructed using a Discrete Fourier Transform (DFT; e.g., Oppenheim & Shafer 1975). The periodogram was constructed from the DFT using the normalization of van der Klis (1997). Periodograms for the revolution 371 and 372 data were constructed separately (e.g., the two orbits were not combined into a single light curve).

Following Papadakis & Lawrence (1993), each periodogram was binned every factor of 1.4 in temporal frequency (0.15 in the logarithm), with the lowest three frequency bins widened to accommodate a minimum of two periodogram points. The resulting PSDs spanned 1.10×10^{-5} Hz – 3.39×10^{-4} Hz and 1.15×10^{-5} Hz – 3.39×10^{-4} Hz for revolutions 371 and 372, respectively, factors of ~1.5 orders of magnitude in dynamic range.

We note that for light curves binned to 200 s, the resulting periodograms were dominated at the highest temporal frequencies (above ~4×10^{-4} Hz) by white noise power due to Poisson noise, confirming the need to rebin the light curves to 1200 s. For all periodograms, the observed white noise power level was equal to the predicted level of power due to Poisson noise (listed in Table 1).

Two methods were used to probe the energy dependence of the high-frequency PSDs. First, the Monte Carlo method of Uttley, M\(^c\)Hardy & Papadakis (2002) was used to quantify the intrinsic, underlying PSD slope, hereafter referred to as $-\beta$. Second, a Monte Carlo method that uses a least-squares fit to the observed (not underlying) PSD was used to probe relative high-frequency slope differences.

3.3.1. *The Underlying PSD slope*

The observed, binned PSDs had poorly defined errors due to the low number of periodogram points in each PSD bin (e.g., Papadakis & Lawrence 1993). Furthermore, the PSDs suffered from the systematic distortion effect of red-noise leak, whereby variability trends on time scales longer than the observed duration can contribute

additional variance to the observed light curve and contribute extra, "leaked" variability power to the observed PSD (e.g., van der Klis 1997). The PSD distortion effect of aliasing is a frequent issue in PSD measurement; with aliasing, discrete, non-continuous sampling fails to distinguish variability trends on time scales longer and shorter than the sampling time and effectively adds extra variability power to the observed PSD. However, aliasing was not expected to be a factor here because these PSDs were derived from continuously sampled data.

We employed the Monte Carlo fitting procedure of Uttley, M\(^c\)Hardy & Papadakis (2002) to get rid of distortion effects, properly assign errors, and quantify the underlying PSD shape. In this procedure, a test model PSD shape is assumed, and a large number (N, at least 100) of light curves are simulated using the method of Timmer & König (1995). The light curves are simulated with a duration much longer than the observed duration to ensure that the light curves account for variability on time scales longer than the observed duration (that is, they contain a variability contribution due to red noise leak). They are also simulated with a time resolution higher than the observed sampling time. The simulated light curves are then resampled to match the observed light curves to ensure that the effects of sampling are identical for both the observed and simulated light curves. The N PSDs are measured from the simulated data and averaged to form an "average distorted model" PSD with well-determined errors, and so-called because they suffer from the aforementioned distortion effects. Finally, the observed PSD is compared to the distribution of the N PSDs to estimate the confidence for the null hypothesis that the specified PSD model shape is correct. For further details of this analysis see §3–4 of Uttley, M\(^c\)Hardy & Papadakis (2002) or §3 of M03.

For the present analysis, the PSD model shape tested was an unbroken power law of the form

$$P(f) = A(f/f_0)^{-\beta} + P_{\mathrm{Psn}}$$

where the normalization A is the PSD amplitude at the break frequency f_0, β is the power law slope, and P_{Psn} is the constant level of power due to Poisson noise. The limited dynamic range of the data precludes testing more complicated PSD model shapes. P_{Psn} was added to the model as opposed to being subtracted from the data, to avoid the possibility of obtaining unphysical negative powers.

The range of β tested was 1.00–4.00 in increments of 0.05. The break frequency was fixed at 4.0×10^{-6} Hz in all cases, though the normalization A was allowed to vary. Light curves were simulated with a duration 250 times the observed duration, to account for red noise leak. The light curves were simulated with a time resolution of 200 s, then binned to 1200 s (1600 s for the MOS2 data). The light curve durations were trimmed to 129.9 ksec or 123.8 ksec for revolutions 371 and 372, respectively. The simulated light curves were resampled to match the observed light curves: 4 data points in the revolution 371 data from 57.0 ksec to 61.8 ksec after the start of the observation were destroyed and linearly interpolated from adjacent points. Of the simulated PSDs, 250 were used to determine the the "average distorted model" PSD with well-defined errors, and 10^3 randomly selected sets of PSDs were used to

probe the simulated χ^2 distribution. Because the power due to Poisson noise differs slightly between the two revolutions, the PSD model shape was fitted separately to the observed PSD for each revolution, with the respective χ^2 values from each revolution added to form a total χ^2 used in determining the goodness of fit.

The best-fit values of β and A, along with the corresponding likelihood of acceptance (defined as $1 - R$, where R is the rejection confidence), are listed in Table 2. Following M03, the uncertainties on β correspond to values 1σ above the likelihood of acceptance for the best-fit value on a Gaussian probability distribution (i.e., the amount β has to change for the fit to be less likely by 1σ). The errors on A were determined from the rms spread of 10^3 randomly selected sets of simulated PSDs. The best-fit PSD model shapes are illustrated in Figure 3. The hard band results are consistent with those presented in M03 for the high-frequency PSD shape derived from 2–10 keV *Chandra* observations.

Due to the limited dynamic range of these PSDs, the Monte Carlo procedure yields very poor constraints on both the high-frequency PSD slope β and the amplitude A. Furthermore, upper limits on β cannot be constrained, for two reasons. First, the presence of a constant Poisson power level dominates the steepest PSD slopes tested, leading to a degeneracy such that most values of $\beta \gtrsim 3$ yield similar rejection probabilities. Second, excessive red-noise leak from very steep PSD slopes increases the PSD errors, with the result that such large errors decrease the reliability of the values of the rejection probability (e.g., M03). Formally, then, we have only lower limits to β. However, looking at the best-fit results, we cannot rule out consistency with previous results that showed that the PSD slope flattens as energy increases. Although the PSD amplitude A at the break is also poorly constrained, the best-fit values are not inconsistent with the amplitude decreasing as photon energy increases.

3.3.2. *Relative differences in PSD slope*

Complementary to finding constraints on the intrinsic slope β using the Monte Carlo procedure above, a power-law model was directly fit to the observed, "raw" PSDs. This was done to obtain additional constraints on β as a function of energy, since the Monte Carlo routine above was not able to provide tight constraints on β given the limited dynamic range of the PSDs. This procedure did not aim to directly identify the underlying high-frequency PSD slope β, but rather to qualitatively identify PSD power-law slopes relative to each other in the presence of red noise leak.

We used a power-law model shape of the same form as in the Monte Carlo analysis,

$$P(f) = A(f/f_0)^{-\beta_{\rm obs}} + P_{\rm Psn}$$

where $\beta_{\rm obs}$ refers to the "raw," observed PSD slope, which is systematically affected by red noise leak. The effect of red-noise leak is to add an f^{-2} noise component to a PSD, thus flattening any intrinsic PSD with power-law slope steeper than –2 (van der Klis 1997). We fit using a "least-squares" routine, specifically, the "GRIDLS" procedure of Bevington (1969), and using the PSD errors assigned from the best-fit model PSDs constructed during the Monte Carlo procedure above. Because $P_{\rm Psn}$ differed

slightly between the two revolutions, the revolution 371 and 372 PSDs were again fit separately for each revolution, with the respective χ^2 values from each revolution added to form a total χ^2 used in determining the goodness of fit. The best fitting slopes and normalizations are summarized in Table 3. However, values of χ^2 are very low due to the large PSD error sizes and the limited dynamic range. The best-fit values for $\beta_{\rm obs}$ tend to flatten as energy increases, consistent with the results of the Monte Carlo fitting above, but the reader is reminded that due to the presence of red-noise leak, these slopes are NOT direct estimates of the underlying PSD model parameters. This contrasts with the results from the Monte Carlo analysis (Table 2 and Figure 3), which show best-fit estimates to the underlying, intrinsic PSD model shape.

The exact amount of power "leaked" from below $f_{\rm min}$ (defined as $1/D$, where D is the observation duration) to above $f_{\rm min}$ is a stochastic quantity, but the amount of red noise leak power present in the observed PSDs can be estimated by integrating the underlying, intrinsic PSD model shape. We used the best-fit doubly-broken PSD model of NGC 3783 from M03,

$$P(f) = \begin{cases} A_l, & f \le f_l \\ A(f/f_h)^{-1}, & f_l < f \le f_h \\ A(f/f_h)^{-\beta}, & f > f_h \end{cases}$$

where A_l is the PSD amplitude below the low-frequency break $f_l = 2\times10^{-7}$ Hz, where the PSD has zero slope. The quantity $A = A_l(f_h/f_l)^{-1}$ is the PSD amplitude at the high frequency break $f_h = 4\times10^{-6}$ Hz. Values of β and A were the slopes and power amplitudes from the best-fit Monte Carlo results in §3.3.1. We assumed that the only PSD model parameters that vary between bandpasses are β and A. We also assumed that the PSD of NGC 3783 does not exhibit non-stationarity between any of the observations, a hypothesis tested in §3.3.3 below. Integration over temporal frequencies from 4×10^{-8} Hz (the temporal frequency corresponding to 250 times the duration of the pn light curves) to 1×10^{-5} Hz (the minimum temporal frequency sampled here) showed that the predicted power due to red noise leak is highest in the soft band and lowest in the hard band, with a factor of 3.2 greater in the soft band compared to the hard band. The relatively softer PSD slopes have thus been flattened to a greater degree relative to harder bands; given that the $\beta_{\rm obs}$ steepen toward higher energies, the intrinsic PSD slopes must also steepen towards higher energies.

Finally, the differences in the best-fit $\beta_{\rm obs}$ between the soft, medium and hard bands were calculated: $\Delta\beta_{\rm obs,S-M} = 0.31$, $\Delta\beta_{\rm obs,S-H} = 0.49$, and $\Delta\beta_{\rm obs,M-H} = 0.19$, where e.g., $\Delta\beta_{\rm obs,S-H}$ equals $|\beta_{\rm obs}|$ for the soft band minus $|\beta_{\rm obs}|$ for the hard band. A Monte Carlo simulation procedure was done to assess the significance of each of these three slope differences. This procedure tested the null hypothesis of simultaneous light curves in two different bandpasses intrinsically having identical underlying PSD shapes and unity coherence (see §3.5 for a definition of coherence). Rejection of this null hypothesis at high confidence would mean that in the limit of unity coherence, the two light curves are derived from underlying PSDs with different shapes. In this Monte Carlo procedure, for each pair of relatively soft and hard light curves, underlying PSD shapes were assumed: the model PSD shape used was the same as

in the Monte Carlo procedure in §.3.3.1. Identical power-law slopes were assumed for both light curves; values of β from 1.0–4.0 were tested in increments of 0.1. For each revolution, 200 light curves were simulated for both the relatively soft and hard bands using the same random number seed to ensure unity coherence between them. Light curves were simulated with a duration 250 times the observed duration in each revolution to adequately ensure the presence of long-term variability trends associated with red noise leak. The time resolution for the simulations was 200 s. The soft and hard light curves were clipped to the appropriate duration (129.9 ks and 123.8 ksec for revolutions 371 and 372, respectively) and binned to 1200 s. The simulated light curves were resampled to match the observed light curve (four flux bins were removed from the revolution 371 soft and hard simulated light curves at 57.0–61.8 ksec after the start of the observation and linearly interpolated). The light curves were rescaled to match the mean count rate and excess variance of the observed light curves. This rescaling accounts for the difference in the expected amount of red noise power leakage between the different bandpasses. PSDs were measured in the same manner as the observed data. PSD errors for the simulations were taken from the best-fit corresponding average distorted model from the Monte Carlo procedure described in §3.3.1. To simulate the effect of Poisson noise in the simulated light curves, each flux point was randomized according to the Poisson distribution. Least-squares fitting was done in the same manner as the observed PSDs, using the same model shape, a red-noise power law plus a white noise component due to Poisson noise. The difference in resulting slopes, e.g., $\Delta\beta_{\rm sim,E1-E2}$ was calculated, where E1 and E2 represent the relatively softer and harder light curves, respectively. A distribution of $\Delta\beta_{\rm sim,E1-E2}$ was formed from the 200 sets of simulations for each test value of β; the distribution arose due to stochastic differences in measured PSD slope from one simulated light curve to the next and due to the minor systematic effects of Poisson noise, but could not be due to differences in intrinsic PSD slope. The $\Delta\beta_{\rm sim,E1-E2}$ distribution was then compared against the observed values of $\Delta\beta_{\rm obs}$. The observed value of $\Delta\beta_{\rm obs,S-M}$ was never reached more than twice in any of the 200 simulations for any initial value of β. Similarly, the observed value of $\Delta\beta_{\rm obs,S-H}$ was never reached more than once out of the 200 simulations for any initial value of β, and $\Delta\beta_{\rm obs,M-H}$ was never reached more than 3 times out of 200 simulations. We can thus reject at 99.5% confidence the null hypothesis of both the S-band and M-band light curves having identical intrinsic PSD shapes in the limit of unity coherence; corresponding rejection confidences for the soft–hard and medium–hard combinations are >99.5% and 98.5%, respectively.

3.3.3. *Stationarity tests*

We tested a fundamental assumption inherent in AGN PSD analysis, that the variability process does not display non-stationarity over long time scales. Following previous definitions, a non-stationary variability process is one whose underlying PSD changes with time. For instance, the PSDs of XRBs change on time scales of hours to days (e.g., Axelsson et al. 2005), but if variability characteristics scale linearly with black hole mass, then one would

not expect AGN PSDs to significantly change shape on time scales less than at least decades to centuries.

Compact accreting black holes display "weakly stationary" behavior in that the mean and variance both show scatter over time, although both the expectation value of the fractional variability amplitude and the underlying PSD shape is expected to remain constant in time (e.g, over time scales shorter than decades). At a given temporal frequency, periodogram values are scattered about the underlying PSD following a χ^2 distribution with two degrees of freedom (e.g., Priestley 1981). For two PSDs that sample the same stationary process and are observed at two different times, the only difference in the PSD values at a given temporal frequency will be due to this scatter. Papadakis & Lawrence (1995) outlined a method to test for non-stationarity (change in underlying PSD shape), defining a statistic S to quantify differences between two PSDs; for a stationary process, S will be distributed with a mean of 0 and a variance equal to 1.

We tested for consistency in PSD shape between the two *XMM-Newton* pn hard band light curves and the five 170-ksec long *Chandra* hard band light curves obtained in 2001 February–June (see M03 and Kaspi et al. 2002 for observing and data reduction details). All light curves were trimmed to a common duration (123.8 ksec, the duration of the rev. 372 light curve) and rebinned to a common sampling time of 2000 s. PSDs were measured using the same normalization as above, and the S-statistic of Papadakis & Lawrence (1995) was calculated. Comparing the revolution 371 and 372 pn PSDs yielded $S = –0.79$. Comparing the revolution 371 PSD to each of the five *Chandra* PSDs yielded S values between –1.50 and –0.58; comparing the revolution 372 PSD to each of the five *Chandra* PSDs yielded S values between –0.71 and +0.21. Finally, comparing each of the *Chandra* PSDs in a pairwise fashion yielded S values between –0.92 and +0.78. All of these values are within 2σ of the expected values assuming stationarity in the data; the assumption of stationarity of the high-frequency power spectrum over time scales of up to ten months is thus a reasonable one.

3.4. *Cross-Correlation Functions*

We next measured the cross-correlation functions (CCFs) to search for intra-X-ray lags. We compared the soft, medium and hard bands in the *XMM-Newton* data, and also compared the H1, H2, H3 and H4 bands to each other in the medium- and long-term data. We used the Interpolated Correlation Function (ICF; White & Peterson 1994), with uncertainties on the ICF peak lag determined using the bootstrap method of Peterson et al. (1998). We also measured the Discrete Correlation Function (DCF; Edelson & Krolik 1988); results were found to be virtually consistent with those obtained via the ICF.

For the short-term data, we used the pn light curves binned to 1200 s (1600 s for the MOS2). Again, only the results for the pn data are presented; the results for the MOS2 data were consistent. DCF and ICF results are summarized in Table 4. ICF results are plotted in Figure 4; the (virtually identical) DCF results are not plotted. Positive lags are defined as relatively harder band variations being delayed with respect to the softer band.

For the short-term data, all peak lags τ are consistent

with delays between 0 and $\lesssim +2$ ksec. Conservatively, one can assign a 2σ limit of twice the mean sampling bin, or $|\tau| \lesssim 2.4$ ksec. The revolution 371 and 372 cross-correlation functions are not identical in profile. However, this difference is not sufficient for any claim of non-stationarity, at least for the hard band, given the results of §3.3.3 above. The cross correlation results reveal an asymmetry towards hard lags at short time scales, especially evident in the revolution 371 data. Such an asymmetry has been seen previously in XRBs (Maccarone et al. 2000) and AGN (McHardy et al. 2004), and is indicative of something more complex than a simple lag that is constant in temporal frequency. There are hints only of positive lags, but moreso in the revolution 371 data, and one cannot definitely conclude that significant lags exist in either short-term data set. For the medium-term and long-term results, peak lags are all consistent with zero; there is no evidence for peak lags outside the (conservative) 2σ lag limits of $|\tau| \lesssim 45.8$ ksec (medium-term) or 8.5 d (long-term).

For all time scales and bandpasses, the peak correlation coefficient r_0 tends to decrease as the relative energy separation between the two bands increases. Monte Carlo simulations were required to assess the significance of this result and distinguish whether it is intrinsic to the source or an artifact due to Poisson noise. The null hypothesis tested was that the two light curves have unity coherence and peak correlation coefficient of 1, with any lack of perfect correlation being due solely to Poisson noise. In these simulations, for each pair of relatively soft and hard light curves, a PSD model shape was assumed. For the short-term data, the best-fit PSD slope and amplitude were taken from the Monte Carlo results of §3.3.1. For the medium- and long-term data, the best fitting doubly-broken PSD model shape of M03 was used. Of the simulated light curves, 200 were simulated for both the relatively soft and hard bands using the same random number seed to ensure unity coherence between them. Light curves were initially generated with a duration 250 times the observed duration. The initial simulated time resolution was 200 s, 2.29 ksec, or 0.43 days for the short-, medium-, or long-term data, respectively; light curves were clipped to the observed duration and resampled to match the sampling of the observed light curves. The light curves were rescaled to match the mean count rate and excess variance of the observed light curves. To simulate the effect of Poisson noise in the simulated light curves, each flux point was randomized according to the Poisson distribution. Cross-correlation peak coefficients r_0 were measured using the ICF as above; these simulated r_0 will be less than 1 due only to the presence of Poisson noise. For each of the 200 pairs of light curves, a distribution of (simulated) r_0 was formed and compared to the observed value of r_0. For all pairs of light curves and time scales, the fraction of simulated values of r_0 exceeded by the observed value of r_0 is listed in Table 4. For the revolution 371 short-term data, the null hypothesis that the two light curves have unity coherence and peak correlation coefficient of 1 is rejected at 91.5% confidence for the soft–hard CCF, and >99.5% confidence for the medium–hard CCF, but cannot be rejected significantly for the soft–medium CCF. For the revolution 372 short-term data, the null hypothesis is rejected at 94.5% confidence for the soft–medium CCF,

97.0% confidence for the soft–hard CCF, and 99.5% confidence for the medium–hard CCF. For the medium-term data, the null hypothesis is rejected at >95.5% confidence for the H1–H2, H1–H3, and H2–H3 CCFs. However, the null hypothesis cannot be rejected at high significance for the H1–H4, H2–H4 and H3–H4 CCFs, due to the lower signal-to-noise in the H4 band. A repeat of this analysis with much larger time bins (e.g., 46 ksec or 92 ksec time bins) would further raise the variability-to-noise ratio of the light curve but would not leave enough data for an adequate CCF. For the long-term data, the null hypothesis is rejected at >99.5% confidence for all CCFs. Overall, there is thus a general consensus that the peak correlation coefficient decreases as the energy separation of the pairs increases.

Autocorrelation functions (ACFs) for the short-term light curves were also calculated using the ICF and DCF; results for the ICF are plotted in Figure 5. The short-term ACFs show a tendency for the central peak to become relatively more narrow at harder energies. This is consistent with the flattening of PSD slope with increasing photon energy as described in §3.3. A similar phenomenon was noted by Maccarone et al. (2000) for Cyg X-1 in the low/hard state.

This energy dependence of the ACF and the high-frequency PSD slope suggest that for a given variability event in Seyfert galaxies or XRBs, the relatively harder X-ray band is associated with shorter rise and decay times. That is, for a phenomenological variability event consisting solely of a rapid flux increase followed by a decrease, the rise and decay times will be shorter for the relatively harder band. However, the sub-band CCF analysis (Figure 4) indicates that the maxima of such events should coincide (to within ~ 2 ksec in the case of NGC 3783). Therefore, one might expect the rise to appear in the softer band first, leading to an increase in the softness ratio (SR), followed by the harder band rising a short time later.

To attempt to provide support for this picure in NGC 3783, CCFs were calculated to search for lags between the SR light curves and the summed flux light curves, e.g., (S/H) versus (S + H). DCF and ICF results are listed in Table 5 and shown in Figure 6, using the same time resolutions as for the earlier CCFs; positive lags are defined as changes in the SR light curve leading changes in the summed light curve. For the short-term data, all peak lags are consistent with delays between ~ 0 and $\sim +8$ ksec, including delays larger than the conservative 2σ limit of 2.4 ksec, e.g., in revolution 371. Formally, the revolution 372 lags are all consistent with zero. For the medium- and long-term data, peak lags are all consistent with zero, with no evidence for lags outside the 2σ limits of 45.8 ksec or 8.5 days, respectively.

One danger inherent in cross-correlation analysis of red-noise light curves is that a small number of large amplitude events or flux changes can dominate the CCF function. For example, in revolution 371, the positive lag may be driven primarily by the big rises in SR and the summed flux at $\sim$ 50–90 ksec after the start of the observation. In revolution 372, the dip and rise in the SR light curves ~ 30 ksec after the start of the observation seems to precede a similar dip and rise about 10 ksec later in the summed light curves. It was therefore necessary to perform Monte Carlo simu-

lations to assess the significance of the SR–summed band lags in the short-term data, the null hypothesis being that the SR light curve and the summed light curves have zero intrinsic lag, and are derived from a pair of relatively soft and hard light curves with unity coherence.

The relatively soft and hard light curves were derived in a manner identical to the CCF simulations above, with the PSD model shapes the same as in §3.3.1, light curve pairs simulated with the same random number seed, and Poisson noise added to the simulated light curves. For each of the 200 pairs of simulated SR and summed light curves, a distribution of simulated lags was formed for comparison with the observed lags. The fraction of simulated positive lags greater than the observed peak lags and the observed lower limits to lags are listed in Table 5.

For revolution 371, the observed peak lag and lower lag limit to the M/H SR versus summed CCF are exceeded by 4/200 and 18/200 simulated lags, respectively, so the null hypothesis is rejected at >90% confidence. For the S/M and S/H ratios in revolution 371, the lower limit to the observed lag is exceeded by at least 40 of 200 simulated lags, so the null hypothesis cannot be rejected at high confidence. For revolution 372, all peak lags are exceeded by 52–56 of 200 simulated lags, and all lag lower limits are exceeded by 105–106 of 200 simulated lags, so the null hypothesis cannot be rejected at high confidence. We conclude that the observation of changes in the softness ratio leading changes in the summed light curve by $\sim$5 ksec is tentative at best.

3.5. *Cross-spectral Properties*

In addition to using the CCF, interband correlations can be characterized using the cross-spectrum; analogous to the fact that the PSD is the Fourier transform of the ACF, the cross-spectrum is the Fourier transform of the CCF. The cross-spectrum is a complex number. Its squared magnitude is used to define the coherence, which is defined and discussed in §3.5.1. The argument of the cross-spectrum is the phase spectrum, which is defined and discussed further in §3.5.2. Further details of the cross-spectrum can be found in e.g., VFN03 and Papadakis, Nandra & Kazanas (2001).

3.5.1. *Coherence Function*

The coherence function $\gamma^2(f)$ gives the fraction of mean-squared variability of one time series that can be attributed to the other, at a given temporal frequency. If the two time series are related by a simple, linear transfer function, then they will have unity coherence. The coherence is defined as the magnitude squared of the cross spectrum normalized by the product of each light curve's PSD. Here, we use the discrete versions of the cross-spectrum and coherence functions, given in §5.2.2 of VFN03. To reduce scatter, the coherence is calculated by averaging the real and imaginary components of the cross-spectrum and the auto-spectra over m consecutive frequencies, assuming that the estimates at each temporal frequency are independent. We correct the coherence function for the influence of Poisson noise by following Vaughan & Nowak (1997). Their equation 8 gives the noise-corrected coherence and its uncertainty. However, it is applicable only in the condition of high coherence and high powers; more

specifically, the intrinsic variability power must be at least a factor of a few times $\sqrt{m} \times P_{\mathrm{Psn}}$. For this condition to be met, it was necessary to rebin the short-term light curves to 5000 sec. For the two short-term light curves, the cross-spectrum and PSD estimated were calculated for each revolution separately, then combined and sorted by frequency before binning.

For the short-term data, the coherence function was calculated for the soft–medium, soft–hard, and medium–hard bands, as well as for H1–H2 and H2–H3. For the medium- and long-term data, the coherence function was measured for all combinations of the H1, H2, H3 and H4 light curves. The long-term coherence functions represent the longest time scale coherence functions measured for an AGN to date. The temporal frequencies sampled span an order of magnitude above and below the high- and low-frequency PSD breaks modeled by M03. Coherence was binned to reduce scatter for all three time scales. The value of m was usually 15, but increased slightly to 20 for coherence functions measured from pairs of light curves that included the (relatively noisy) H4 band. This yielded only one coherence estimate for the medium-term data and two coherence estimates for the short-term data, but 7–9 estimates for the long-term data.

The combined results, spanning the temporal frequency range $6 \times 10^{-8} - 1 \times 10^{-4}$ Hz, are shown in Figure 7. We note that the uncertainties on the coherence points, calculated using the formulation of Vaughan & Nowak (1997), are in general agreement with the scatter of the unbinned coherence estimates (not plotted); scatter is generally larger for relatively lower coherence estimates. This suggests that the coherence estimates are reasonably accurate. Overall, on the temporal frequencies sampled, the measured coherence of the light curves is relatively close to unity. However, the coherence has a tendency to decrease somewhat as the relative separation of the two energy bands increases. This appears consistent with what was observed in the CCFs (§3.4). However, Poisson noise could play a role, artificially reducing the measured coherence.

As a preliminary check on the accuracy of the short time scale coherence measurements, coherence functions were also calculated using the MOS2 data. At the lowest frequency bin, the coherence functions derived from the MOS2 data agree with those derived from the pn data. However, the high level of Poisson noise in the MOS2 data prevents further comparison at higher temporal frequencies. As another check on the accuracy of the short time scale coherence measurements, the coherence was calculated between the MOS2 and the pn for each of the soft, medium, and hard bands. Because the light curves extracted from either detector should be identical except for the effects of Poisson noise, any deviation from unity coherence would have to be due to Poisson noise. At frequencies lower than about 10^{-4} Hz, the coherence is indeed close to 1 (not plotted).

Monte Carlo simulations were used as an additional check on the accuracy of the coherence estimates and to determine if any deviation from unity coherence can be attributed to the effect of Poisson noise. Simulations were performed for each time scale separately. Two light curves were simulated using the same random number seed and

identical PSD shapes, to produce two light curves with intrinsic unity coherence. The best-fit medium-band high-frequency PSD slope and amplitude was assumed. The simulated light curves for the two bands were resampled to match the observed data, and rescaled to the mean count rates in the softer and harder bands. Poisson noise was then added to the data according to the Poisson distribution (that is, randomly deviating the data using a Gaussian convolved with the square root of the observed mean error squared). One hundred sets of simulated data were produced. For each set, the coherence and its uncertainty was calculated as for the real data. At most temporal frequencies (e.g., particularly the long- and medium-term data), the coherence was reasonably close to unity, and the uncertainty in the coherence was in reasonable agreement with the scatter, indicating that the coherence estimation was reasonably accurate. The 90% and 95% lower limits to the coherence were determined, and are plotted in Figure 7. Any measured coherence point lying below these lines thus indicates a drop in coherence that is intrinsic to the source, and not an artifact of the Poisson noise, at 90% or 95% confidence. For most temporal frequencies, the artificial drop in coherence is small. At most temporal frequencies, particularly below $\sim 10^{-6}$ Hz, the deviation of the measured coherence from unity is greater than the artificial drop due to Poisson noise at greater than 95% confidence. Furthermore, there is a general tendency for the intrinsic coherence to decrease as the energy separation of the bands increases.

Previous analysis (§3.3) has shown that the high-frequency PSD slope in NGC 3783 is consistent with being energy-dependent; such a dependence could contribute to a reduction in measured coherence. However, assuming that the PSD break frequencies change, and assuming that the power-law slopes below the high-frequency break do not change, any putative change in high-frequency slope will not have any effect on the coherence below 4×10^{-6} Hz in NGC 3783. The Monte Carlo simulations were repeated exactly as above for the short-term data, but using the best-fit PSD slopes and amplitudes from §3.3.1, and for the medium-term data, assuming power law slopes of –2.3, –2.2, –2.1, and –2.0 for the H1, H2, H3 and H4 bands, respectively. The effects of Poisson noise were again added to the simulated data. The drop in coherence due to having different high-frequency PSD slopes was minimal for all bandpass combinations, and virtually insignificant compared to the drop in coherence due to Poisson noise (not plotted).

We can conclude that the coherence is reasonably close to unity over the temporal frequencies sampled, but there are deviations from unity coherence present that are greater than those introduced by Poisson noise or by having different high-frequency PSD slopes. The fact that the coherence tends to drop as the energy separation of the bandpasses increases is consistent with the CCF results from §3.4.

3.5.2. *Phase Lags*

The phase spectrum indicates the average phase shift between the components of the two light curves, as a function of temporal frequency. Phase lag analysis is complementary to CCF analysis band light curves), as the two

methods are sensitive to the variability on different time scales. CCFs tend to be most sensitive to the largest amplitude variations in a time series, which, for red noise processes, will be those on relatively larger time scales (10 ksec and longer in the case of the *XMM-Newton* light curves studied here). Phase lag analysis, meanwhile, is more sensitive to the variations on relatively smaller time scales after accounting for binning as described below (hundreds of seconds in this case). However, sensible results for phase lag measurement requires data of sufficiently high quality. For instance, one requires continuous or near-continuous sampling to recover phase lags that are a small fraction of the total duration. The medium- and long-term sampling light curves, for instance, each span only ~ 2 dex in temporal frequency, and the sparse sampling at the lowest temporal frequencies is insufficient to recover e.g., phase lags that are a small fraction (a few percent) of the total duration. Consequently, here we concentrate on recovering phase lags from the short-term data only. Additionally, the coherence must be high (the variations in the two bands must be reasonably well-correlated) for lags to be meaningful. In the case of NGC 3783, phase lags are only recoverable in the narrow temporal frequency range of $6 \times 10^{-5} - 1.3 \times 10^{-4}$ Hz.

We follow section 5.3.1 of VFN03 to estimate the phase lags from the short-term light curves for NGC 3783. We combined unbinned data from revolutions 371 and 372 and sorted by frequency. Phase lag estimates were binned over 20 consecutive temporal frequencies to reduce scatter. The phase lags $\phi(f)$, along with their uncertainties $\Delta\phi$, which were determined from equation 16 of Nowak et al. (1999a), are plotted in Figure 8. A positive lag is defined as relatively soft band variations preceding those in the hard band. There is approximate closure in the resulting phase lags: the sum of the S–M and M–H phase lags at a given frequency bin is roughly equal to the S–H phase lags. There are only two frequency bins, but the data are not inconsistent with phase lags increasing as the energy separation of the bands increases and as temporal frequency increases, qualitatively consistent with the previous phase lag studies of AGNs and XRBs. The dependence on temporal frequency explains the asymmetry present in the CCFs; this phenomenon has been noted previously by e.g., Maccarone et al. (2000) and McHardy et al. (2004). The error on the phase lags was seen to be in reasonable agreement with the scatter of the unbinned phase lag estimates at these frequencies, indicating that the formulations used here for ϕ and $\Delta\phi$ are reasonable. The phase lags are consistent with being described by the relation $\phi(f) = Cf^{-1.2}$, where $C \sim 0.001$, 0.003, and 0.004 for the S–M, M–H, and S–H lags, respectively, although these relations are obviously poorly constrained due to the narrow range of temporal frequencies sampled. The relation between phase lags and temporal frequency has been quantified in previous studies (see references above) as $\phi(f) = Cf^{-1}$; in this case, the best-fit f^{-1} relation yields $C \sim 0.009$, 0.026, and 0.036 for the S–M, M–H, and S–H lags, respectively.

We follow section 4.2 of Nowak et al. (1999a) to estimate the effective noise limit; their equation 14 yields the lower limit on the uncertainty on the phase lags due to the presence of Poisson noise. These limits as a function

of frequency were calculated for each bandpass pair using the average of the best-fit PSD shapes from §3.3.1 (e.g., assume $\beta = 2.9$ for S–M, etc.), and the average of the power due to Poisson noise from both bands and both revolutions of data. The measured coherence is consistent with, and assumed to have the form of $\gamma^2(f) = exp(-f/10^{-3.8}Hz)^2$; the cutoff frequency was chosen somewhat arbitrarily and given the results of §3.5.1. These limits are shown in Figure 8, and indicate that phase lags cannot be recovered from the data at temporal frequencies above $\sim 10^{-3.8}$ Hz.

Phase lags were also recovered for the H1–H2, H2–H3, and H1–H3 bandpass pairs, but due to an even narrower usable temporal frequency range, this analysis yielded only one binned phase lag point for each pair. The phase lags obtained, at a binned frequency of 4.33×10^{-5} Hz, were reasonably consistent with closure: $\phi(f) = 300\pm10$ s for the H1–H2 bands, $\phi(f) = 500\pm30$ s for the H2–H3 bands, and $\phi(f) = 800\pm50$ s for the H1–H3 bands. The detection limits due to Poisson noise were in the vicinity of 10, 30, and 50 seconds for the H1–H2, H2–H3, and H1–H3 bands, respectively. The MOS2 data were tested for consistency, but found to be too noisy for phase lags to be recovered.

Monte Carlo simulations, similar to those performed for the coherence functions above, were performed as an additional verification of the phase lag estimates. One hundred pairs of light curves were simulated, with each pair simulated with the same random number seed and same underlying PSD shape to ensure that they have unity coherence, identical Fourier phases, and no intrinsic lag. Poisson noise was added to the simulated light curves as described in §3.5.2. Phase lags were measured in a manner identical to the real data. The resulting simulated phase lags were reasonably close to zero, indicating that the observed phase lags are not an artifact due to Poisson noise. Simulations were also performed with light curves derived from different underlying PSD slopes. The resulting simulated phase lags were again close to zero, suggesting that the energy-dependent PSD shape did not bias the phase lag results.

4. DISCUSSION AND CONCLUSIONS

4.1. *Summary of observational results*

We have presented several probes of the energy-dependence of the variability properties of the Seyfert 1 galaxy NGC 3783, using complementary *RXTE* monitoring and *XMM* long-looks to quantify the variability over a broad range of time scales. We find relatively softer energy bands to display higher amplitudes of variability on all time scales, in line with numerous previous results. On short time scales, we find that the high-frequency PSD slope is consistent with flattening as photon energy increases. Consequently, the central peak of the ACFs narrower as photon energy increases. Cross-correlation functions show peaks near zero lag, but with a slight asymmetry in the sense that the CCFs are skewed towards positive lags. The peak correlation coefficient decreases slightly as the energy separation of the bands increases. The hardness ratio is generally correlated with the continuum flux, consistent with spectral softening as flux increases, as is commonly seen in Seyferts. However, cross-correlation measurements of the SR versus the summed band tentatively reveal an indication for the softening to precede

the brightening by very roughly 5 ksec. The broadband coherence function is close to unity in the frequency range $6 \times 10^{-8} - 1 \times 10^{-4}$ Hz; however, the coherence seems to decrease slightly as the energy separation of the bands increases. The temporal frequency dependence of the phase lags was explored on short time scales; the data are consistent with phase lag increasing both as the temporal frequency decreases and as the energy separation of the two bands increases; this behavior explains the asymmetrical and skewed shape of the CCF.

4.2. *Comparison to previous results*

All of these results are in qualitative agreement with previous studies of Seyferts and XRBs (See §1 for objects and references), consistent with the notion that XRBs and Seyferts are mass- and/or luminosity- scaled versions of the same accretion phenomenon. However, a detailed comparison between NGC 3783 and XRBs would ideally take into consideration whether NGC 3783 is an analog of an XRB in its low/hard or high/soft state. In terms of broadband PSD shape, NGC 3783 is consistent with the low/hard state of the Galactic black hole candidate Cyg X-1, since both PSDs are not dominated by $1/f$ noise at the lowest temporal frequencies probed (down to $\sim 10^{-8}$ Hz in the case of NGC 3783; also see Axelsson et al. 2005). However, given NGC 3783's black hole mass of $3.0 \pm 0.5 \times 10^7$ M$_\odot$ (Peterson et al. 2004), the high-frequency PSD break of 4×10^{-6} Hz for NGC 3783 is more consistent with linearly scaling with black hole mass from Cyg X-1's high/soft state than from the low/hard state, assuming that both objects accrete at the same rate relative to Eddington. The transition between the low/hard and high/soft states in XRBs usually occurs when the accretion rate is $\sim 2\%$ of Eddington (Maccarone 2003); however, estimating the accretion rate of NGC 3783 does not shed any light on state identification. Given NGC 3783's 2–12 keV luminosity of $\sim 2 \times 10^{43}$ erg s^{-1} (Markowitz & Edelson 2004), the relation between X-ray luminosity and bolometric luminosity L_{Bol} given by Padovani & Rafanelli (1988) of $L_{Bol} = 60 \times \nu L_\nu$ at $\nu = 2$ keV, and a photon index of 1.7 (e.g., Markowitz, Edelson & Vaughan 2003a), the bolometric luminosity is estimated to be $\sim 5 \times 10^{44}$ erg s^{-1} (Note that the factor 27 given as the ratio of L_{Bol} to 2–12 keV luminosity in Markowitz & Edelson 2004 is only valid if the photon index is close to 1.6). Given NGC 3783's black hole mass of 3×10^7 M$_\odot$, this yields an estimate of L_{Bol}/L_{Edd} of roughly 12%. While this value is above the transition threshold in XRBs and implies a high/soft state analogue, it is not immediately reconcilable with PSD shape if the specific analogy to Cyg X-1 is valid. Furthermore, another twist is pointed out by Done & Gierliǹski (2005): the PSDs of transient accreting compact sources (i.e., in contrast to the relatively more stable Cyg X-1) often are not dominated by $1/f$ noise at their lowest frequencies in either their low/hard or high/soft state. Instead of labeling NGC 3783 as a low/hard or high/soft state accretor, it is therefore more conservative to simply say that this paper presents the first measurement of cross-spectral properties at low temporal frequencies for a Seyfert galaxy whose broadband PSD shows evidence for two breaks and is not dominated by $1/f$ noise at the lowest temporal frequencies probed.

NGC 3783's coherence is seen to be close to unity in the vicinity of both the high-frequency and low-frequency PSD breaks, as well as in between these breaks. This is similar behavior to that of the coherence function for Cyg X-1 in the low/hard state (Nowak et al. 1999a). The results so far for objects with both measured coherence and PSD breaks seem to indicate that coherence is reasonably close to unity below the high-frequency break in most objects. This includes Cyg X-1 and GX 339–4 in the low-hard state (Nowak et al. 1999a, 1999b), as well as MCG–6-30-15 and NGC 4051 (VFN03 and McHardy et al. 2004, respectively), though it has been noted that the PSD shapes of these latter two objects are more similar to Cyg X-1 in the high/soft state. The narrow-line Seyfert 1 galaxy Mkn 766 may be a possible exception in this regard, as discussed by Vaughan & Fabian (2003).

Further similarities between NGC 3783 and the low/hard state of Cyg X-1 can be found in the ACFs and CCFs. Maccarone et al. (2000) noted that the FWHMs of the central ACF peaks scaled as $E^{-0.2}$ (E is the photon energy) in the low/hard state of Cyg X-1. The ACF FWHMs for NGC 3783 are roughly 42 ksec, 36 ksec and 26 ksec, respectively, for the S, M and H bands in the revolution 371 data, and roughly 48 ksec, 40 ksec and 34 ksec, respectively, for S, M, and H in revolution 372, and these FWHMs are also consistent with scaling roughly as $E^{-0.2}-E^{-0.3}$. Additionally, Maccarone et al. (2000) noted that the CCF peak lags in Cyg X-1 were less than 2 msec. If we scale by a factor of 3×10^6, the ratio of the black hole masses, one would expect peak CCF lags in NGC 3783 to be within roughly 6 ksec, as observed. However, we note that the CCF (and the ACF) can change character (e.g., FWHMs) quite dramatically from one light curve realization of a given PSD to the next, so a CCF comparison should be regarded with caution. Nonetheless, the data are consistent with the notion of similar variability properties in NGC 3783 and (at least the low/hard state of) Cyg X-1.

4.3. *Physical implications of coherence results*

As explained in Vaughan & Nowak (1997), coherence between two energy bands can be lost if the transfer function is nonlinear, or if there are multiple, uncorrelated transfer functions. In the case of multiple flaring regions (e.g., shot-noise models), if more than one region contributes to the signal in both energy bands, then it is possible for coherence to be low, even if individual regions produce perfectly coherent variability. This is because in order to achieve unity coherence, each separate region independently requires the same linear transfer function that links soft to hard variations. The relevance of coherence to shot-noise models is discussed further in §4.4 below.

The high level of coherence on temporal frequencies below the high-frequency PSD break in NGC 3783 may indicate that the corona is effectively static on these time scales. More specifically, the fact that coherence is high for temporal frequencies near the low-frequency PSD break may indicate that the time scale corresponding to the low frequency PSD break is not directly associated with the dynamic time scale of the corona.

Drops in coherence have been seen at temporal frequencies higher than the high-frequency PSD break in Cyg X-1, MCG–6-30-15, and NGC 4051 (Nowak et al. 1999a, VFN03, McHardy et al. 2004). The corona may be dynamic on those short time scales; that is, the loss of coherence could indicate that these time scales may be directly associated with the formation time scales and/or changes in temperature and/or physical structure of the corona (e.g., Nowak & Vaughan 1996, Nowak et al. 1999a). No such coherence drop is detected in the present data for NGC 3783 due to insufficient variability-to-noise. The highest temporal frequency bin in the short-term data (at 1×10^{-4} Hz) may, at first glance, be suggestive of the beginning of a drop in intrinsic coherence, but the noise-corrected coherence and the simulations show that this drop is instead likely an artifact due to Poisson noise.

4.4. *Phenomenological variability models*

Many models have been invoked to explain the red noise variability properties of Seyferts and XRBs, including shot-noise models (e.g., Merloni & Fabian 2001), rotating hot-spots on the surface of the accretion disk (Bao & Abramowicz 1996), self-organized criticality ("pulse avalanche" models; Mineshige, Ouchi & Nishimori 1994), magnetohydrodynamical instabilities in the disk (Hawley & Krolik 2001), and inwardly-propagating fluctuations in the local accretion rate (Lyubarskii 1997). As noted by e.g., McHardy et al. 2004, shot-noise models can reproduce virtually any red-noise PSD shape. However, on short time scales, shot-noise models have difficulty reproducing the linear relation between rms variability and continuum flux observed in XRBs and Seyferts (Uttley & McHardy 2001, Uttley, McHardy & Vaughan 2005). Furthermore, as discussed in Vaughan & Nowak (1997) and §4.3, shot-noise models lead to low observed coherence unless each separate emitting region independently has the same linear transfer function between soft and hard energy bands. For example, in the "thundercloud" model of Poutanen & Fabian 1999, phase lags could be attributed to the spectral hardening of individual flares (see also Böttcher & Liang 1998), but unity coherence can be achieved only if the exact same Comptonization spectrum and flare evolution independently apply to each flare (Nowak et al. 1999b).

Thermal Comptonization of soft seed photons by a hot corona is a likely explanation for the X-ray emission. It is supported e.g., by X-ray energy spectra, as well as by the correlation between UV flux and X-ray photon index observed in NGC 7469 by Nandra et al. (2000). The phase lags could thus be attributed to the time scale for the seed photons to diffuse through the corona and undergo multiple up-scatterings, and, as discussed by e.g., VFN03, the simplest models predict that hard photons should lag soft photons. However, the simplest Compton models do not predict that the lags should depend on temporal frequency (Miyamoto et al. 1998), as observed. Furthermore, if phase lags do scale with the inverse of the temporal frequency, then extension of this relation to low frequencies would require a non-compact ($\sim 10^{3-5}$ gravitational radii; see Nowak et al. 1999b and Papadakis, Nandra & Kazanas 2001) corona (e.g., Kazanas, Hua & Titarchuk 1997). In addition, Compton scattering models predict that for relatively higher energy photons, which have undergone more scatterings, the most rapid variations will be washed out. This would lead to high-frequency PSD slopes

that steepen as photon energy increases, contrary to observations. However, the energy dependence of the PSD could be obtained with a corona whose temperature increased towards smaller radii (Kazanas, Hua & Titarchuk 1997).

A quantitative model in which inwardly-propagating variations in the local mass accretion rate are responsible for the observed X-ray variability seems to be able to explain many of the observational results in Seyferts and XRBs (Lyubarskii 1997, Churazov, Gilfanov & Revnivtsev 2001), Kotov et al. 2001; see also discussions in VFN03 and McHardy et al. 2004). In this model, variations at a given radius are associated with the local inward propagation time scale, so relatively smaller radii are associated with relatively more rapid variations. Churazov et al. (2001) have suggested a geometrical configuration wherein an optically-thick, geometrically-thin soft disk is sandwiched above and below by an optically-thin corona. The disk is responsible for the bulk of the accretion rate but is not strongly variable; the bulk of the variations occur in the coronal flow. These variations propagate inward until they reach, and modify the emission of, the central X-ray emitting region, yielding a $1/f$ X-ray PSD across a broad range of temporal frequencies (Kotov et al. 2001, Lyubarskii 1997). The most rapid variations are suppressed, leading to a PSD break at high temporal frequencies (e.g., at the frequency f_3 in Figure 3 of Churazov et al. 2001); the break time scale may possibly be associated with the viscous time scale at the edge of the central X-ray emitting region. In the high-soft state, the disk extends down to the central X-ray emitting region. In the low-hard state, the disk is truncated; below the truncation radius, all of the accretion flow is in the form of the corona. Local variations at all radii will contribute to a $1/f$ X-ray PSD. However, variations originating from radii larger than the disk truncation radius are suppressed due to the presence of the non-variable disk. The resulting X-ray PSD follows a $1/f$ relation over two separate ranges of frequencies, but linked by a 'transition region' consisting of an f^0 dependence over some intermediate range of frequencies; variations at these temporal frequencies are not due to local instabilities in the accretion flow but are rather the result of stochastic superposition of variations on shorter time scales. This model thus incorporates two additional PSD breaks at low frequencies, whereby the PSD slope changes from –1 to 0, then back to –1 (temporal frequencies f_1 and f_2 in Figure 3 of Churazov et al. 2001, with $f_1 < f_2$). The "low-frequency break" at $\sim 2 \times 10^{-7}$ Hz in NGC 3783, for instance, could be the characteristic frequency in the coronal flow at the disk truncation radius. The lowest PSD break in this model (f_1), below which the PSD returns to a $1/f$ shape, has not yet been observed in NGC 3783 or any AGN; from scaling with Cyg X-1, it might be expected near $\sim 10^{-9}$ Hz (corresponding to a time scale of ~ 30 years) in NGC 3783. Another common method of modeling XRB PSDs, particularly those in the low/hard

state, is with Lorentzian components; in the context of this class of models, such components could be associated with the corona at radii below the disk truncation radius and thus are absent from the high frequency PSDs of XRBs in the high/soft state. The "two-break" PSD shape for NGC 3783 may actually consist of two Lorentzian components if NGC 3783 is a low/hard state AGN.

The accretion rate variation model class is qualitatively consistent with the rms-flux relation seen in Seyferts and XRBs. In the case of NGC 3783, there is an insufficient flux range on both medium and long time scales to test for the rms-flux relation (the variability is dominated by variations below the high-frequency break), and there is not enough data on short time scales after suitably binning the data. Kotov et al. (2001) suggested that the spectrum can be a function of radius, with relatively harder emission emanating from smaller radii, and therefore associated with more rapid variability; this leads to high-frequency PSD slopes that flatten versus energy. Relatively longer temporal frequencies are associated with larger radii and longer characteristic time scales, hence phase lags are longer. Phase lags increase as the energy separation of the bands increases because the two bands are associated with two radii that are relatively more spatially separated. CCF peak correlation coefficients and coherence both decrease as the energy separation of two bands increases because propagations can only travel inward, and the relatively harder energy band (emitted at a smaller radius) will have undergone additional perturbations. CCF lags are expected to be close to zero, as observed, since the bulk of the X-rays are emitted at very small radii, but the dependence of the phase lags on temporal frequency causes the CCF asymmetry.

Finally, Körding & Falcke (2004) note that a pivoting power-law model seems qualitatively capable of reproducing many of the observed variability characteristics in XRBs (and by extension, Seyferts). This model yields high coherence over a broad range of time scales, ACF peaks which get narrower as energy increases, and phase lags that exhibit a dependency on temporal frequency in a manner similar to those observed.

REFERENCES

Axelsson, M., Borgonovo, L. & Larsson, S. 2005, A&A, 438, 999
Bao, G. & Abramowicz, M. 1996, ApJ, 465, 646
Belloni, T., Homan, J., Casella, P., van der Klis, M., Nespoli, E., Lewin, W.H.G., Miller, J.M. & Mendez, M. 2005, A&A, 440, 207

Beloborodov, A.M. 1999, ApJ, 510, L123
Bevington, P. R. 1969, Data Reduction and Error Analysis for the Physical Sciences (New York: McGraw-Hill)
Böttcher, M. & Liang, E.P. 1998, ApJ, 506, 281

Churazov, E., Gilfanov, M. & Revnivtsev, M. 2001, MNRAS, 321, 759

Done,C. & Gierliǹski, M. 2005, MNRAS, submitted (arXiv: astro-ph/0505183)

Edelson, R. & Krolik, J. 1988, ApJ, 333, 646

Edelson, R. & Nandra, K. 1999, ApJ, 514, 682

Edelson, R. et al. 2002, ApJ, 568, 610

Hawley, J.F. & Krolik, J.H. 2001, ApJ, 548, 348

Kalemci, E., Tomsick, J., Rothschild, R., Pottschmidt, K. & Kaaret, P. 2004, ApJ, 603, 231

Kaspi, S. et al. 2002, ApJ, 574, 643

Kazanas, D., Hua, X.-M. & Titarchuk, L. 1997, ApJ, 480, 735

Körding, E. & Falcke, H. 2004, A&A, 414, 795

Kotov, O., Churazov, E. & Gilfanov, M. 2001, MNRAS, 327, 799

Leighly, K.M. 2004, Prog. Theor. Phys. Suppl., 155, 223

Lin, D., Smith, I.A., Böttcher, M., Liang, E.P. 2000, ApJ, 531, 963

Lyubarskii, Y.E. 1997, MNRAS, 292, 679

McHardy, I.M., Papadakis, I., Uttley, P., Page, M.J. & Mason, K.O. 2004, MNRAS, 348, 783

Maccarone, T. 2003, A&A, 409, 697

Maccarone, T., Coppi, P. & Poutanen, J. 2000, ApJ, 537, L107

Markowitz, A., Edelson, R. & Vaughan, S. 2003a, ApJ, 598, 935

Markowitz, A. et al. 2003b, ApJ, 593, 96 (M03)

Markowitz, A. & Edelson, R. 2004, ApJ, 617, 939

Markowitz, A. & Uttley, P. 2005, ApJL, 625, L39

Marshall, K., Ferrara, E.C., Miller, H.R., Marscher, A.P. & Madejski, G. 2004, proceedings of "X-Ray Timing 2003: Rossi and Beyond," eds. P. Kaaret, F.K. Lamb, & J H. Swank (Melville, NY: American Institute of Physics) (astro-ph/0312422)

Merloni, A. & Fabian, A.C. 2001, MNRAS, 328, 958

Mineshige, S., Ouchi, N.B. & Nishimori, H. 1994, PASJ, 46, 97

Miyamoto, S., Kimura, K., Kitamoto, S., Dotani, T. & Ebisawa, K. 1991, ApJ, 383, 784

Miyamoto, S. & Kitamoto, S. 1989, Nature, 342, 773

Miyamoto, S., Kitamoto, S., Mitsuda, K. & Dotani, T. 1988, Nature, 336, 450

Nandra, K., Le, T., George, I.M., Edelson, R., Mushotzky, R.F., Peterson, B.M., Turner, T.J. 2000, ApJ, 544, 734

Nandra, K. & Papadakis, I. 2001, ApJ, 554, 710

Nowak, M. & Vaughan, B. 1996, MNRAS, 280, 227

Nowak, M., Vaughan, B., Wilms, J., Dove, J., & Begelman, M. 1999a, ApJ, 510, 874

Nowak, M., Wilms, J., & Dove, J. 1999b, ApJ, 517, 355

Oppenheim, A. & Shafer, R. 1975, "Digital Signal Processing," (Prentice-Hall Publishing)

Padovani, P. & Rafanelli, P. 1988, A&A, 205, 53

Papadakis, I. & Lawrence, A. 1993, MNRAS, 261, 612

Papadakis, I. & Lawrence, A. 1995, MNRAS, 272, 161

Papadakis, I., Kazanas, D. & Akylas, A. 2005, ApJ, 631, 727

Papadakis, I., Nandra, K. & Kazanas, D. 2001, ApJ, 554, L133

Papadakis, I., Petrucci, P.O., Maraschi, L., McHardy, I.M., Uttley, P. & Haardt, F. 2002, ApJ, 573, 92

Peterson, B.M. et al. 1998, PASP, 110, 660

Peterson, B.M. et al. 2004, ApJ, 613, 682

Poutanen, J. & Fabian, A.C. 1999, MNRAS, 306, L31

Priestley, M. 1981, "Spectral Analysis and Time Series," (London: Academic Press Ltd.)

Rodriguez, J., Corbel, S., Kalemci, E., Tomsick, J. & Tagger, M. 2004, ApJ, 612, 1018

Shapiro, S., Lightman, A. & Eardley, D. 1976, ApJ, 204, 187

Stern, B.E., Poutanen, J., Svensson, R., Sikora, M. & Begelman, M. 1995, ApJ, 449, L13

Struder, L. et al. 2001, A&A, 365, L18

Svensson, R. 1996, A&AS, 120, 475

Swank, J. 1998, in Nuclear Phys. B (Proc. Suppl.): The Active X-ray Sky: Results From BeppoSAX and Rossi-XTE, Rome, Italy, 1997 October 21-24, eds. L. Scarsi, H. Bradt, P. Giommi, & F. Fiore, Nucl. Phys. B Suppl. Proc. (The Netherlands: Elsevier Science B.V.), 69, 12

Sunyaev, R. & Titarchuk, L. 1980, A&A, 86, 121

Timmer, J. & König, M. 1995, A&A 300, 707

Turner, M.J.L. et al. 2001, A&A, 365, L27

Uttley, P. & McHardy, I.M. 2001, MNRAS, 323, L26

Uttley, P., McHardy, I.M. & Papadakis, I.E. 2002, MNRAS, 332, 231

Uttley, P., McHardy, I.M. & Vaughan, S. 2005, MNRAS 359, 345

van der Klis, M. 1997, in Statistical Challenges in Astronomy II, ed. G.J. Babu & E.D. Feigelson (New York: Springer), 321

van der Klis, M. 2004, to appear in "Compact stellar X-ray sources," Lewin & van der Klis (eds.), Cambridge Univ. Press (astro-ph/0410551)

Vaughan, B. & Nowak, M. 1997, ApJ, 474, L43

Vaughan, S., Edelson, R., Warwick, R. & Uttley, P. 2003a, MNRAS, 345, 1271

Vaughan, S. & Fabian, A. 2003, MNRAS, 341, 496

Vaughan, S., Fabian, A. & Nandra, K. 2003b, MNRAS, 339, 1237 (VFN03)

Vaughan, S. & Uttley, U. 2005, MNRAS, 362, 235

White, R. & Peterson, B.M. 1994, PASP, 106, 879

Zdziarski, A., Lubinski, P., Gilfanov, M. & Revnivtsev, M. 2003, MNRAS, 342, 355

Zdziarski, A., Lubinski, P. & Smith, D.A. 1999, MNRAS, 303, L11

TABLE 1
SOURCE AND DERIVED VARIABILITY PARAMETERS

Time Scale	N	Bandpass (keV)	Mean ct s^{-1}	S/N	P_{Psn} (Hz^{-1})	F_{var} (%)
Short (Rev. 371)	108	0.2–12	9.05	102.3	0.22	15.2 ± 0.1
		0.2–0.7	2.57	54.7	0.80	20.4 ± 0.2
		0.7–2	3.71	66.1	0.55	15.4 ± 0.1
		2–12	2.78	57.0	0.73	10.9 ± 0.2
		2–4	1.37	40.1	1.47	12.2 ± 0.2
		4–7	1.09	36.1	1.85	9.9 ± 0.3
		7–12	0.41	25.1	4.96	5.5 ± 0.4
Short (Rev. 372)	103	0.2–12	12.42	121.4	0.16	12.9 ± 0.1
		0.2–0.7	3.63	65.9	0.55	15.9 ± 0.2
		0.7–2	5.11	78.4	0.39	13.0 ± 0.1
		2–12	3.70	66.6	0.54	10.7 ± 0.1
		2–4	1.86	47.1	1.08	11.7 ± 0.2
		4–7	1.42	41.4	1.41	9.8 ± 0.2
		7–12	0.48	26.5	4.15	5.9 ± 0.4
Medium	151	2–18	6.84	42.2	6.18	11.9±0.2
		2–12	6.33	42.5	6.18	12.1±0.2
		2–4	1.61	22.8	23.4	13.9±0.4
		4–7	2.77	29.1	13.1	11.9±0.3
		7–12	1.95	22.4	23.0	11.0±0.4
		12–18	0.51	8.4	166	9.4±1.5
Long	281	2–18	7.86	62.4	114	21.0±0.1
		2–12	7.28	62.4	114	21.3±0.1
		2–4	1.88	33.7	428	24.5±0.2
		4–7	3.21	44.8	243	21.6±0.2
		7–12	2.18	32.8	439	19.0±0.2
		12–18	0.58	12.7	3010	18.7±0.6

Note. — Values are for the *XMM-Newton* pn (short-term) and *RXTE* (medium- and long-term) data. The *XMM-Newton* pn data has been binned to 1200 s. N (Col. [2]) is the number of points in each light curve. For Col. (4), the entries in the medium- and long-term rows refer to *RXTE* mean count rate per PCU. Col. (5) is the average signal-to-noise. Col. (6) is the expected power due to Poisson noise.

TABLE 2
RESULTS FOR MONTE CARLO PSD FITTING

Bandpass (keV)	Best-fit β	Best-fit A (Hz^{-1})	Likelihood of acceptance
0.2–12	$2.60^{+1.40}_{-0.80}$	$7.2^{+2.6}_{-1.8} \times 10^3$	0.84
0.2–0.7	$3.15^{+0.85}_{-0.80}$	$13.9^{+6.1}_{-4.4} \times 10^3$	0.55
0.7–2	$2.60^{+1.40}_{-0.95}$	$8.5^{+3.0}_{-2.2} \times 10^3$	0.87
2–12	$2.20^{+0.80}_{-0.65}$	$4.3^{+1.2}_{-1.0} \times 10^3$	0.95

Note. — Results from fitting the PSDs with an unbroken power law model (i.e., a break at 4.0×10^{-6} Hz, below the minimum frequency sampled here). A is the amplitude at the 4.0×10^{-6} Hz break. Upper limits to β are not constrained.

TABLE 3
RESULTS FOR χ^2 PSD FITTING

Band (keV)	Best-fit β_{obs}	Best-fit A (Hz^{-1})	χ^2/d.o.f.
0.2–12	2.43±0.05	$12.9^{+4.9}_{-3.6} \times 10^3$	4.0 / 16
0.2–0.7	2.70±0.06	$24.5^{+11.8}_{-7.9} \times 10^3$	5.3 / 16
0.7–2	2.40±0.05	$13.2^{+5.0}_{-3.7} \times 10^3$	3.7 / 16
2–12	2.21±0.04	$7.4^{+2.4}_{-1.8} \times 10^3$	4.5 / 16

Note. — Results of least-squares fitting to the observed *XMM-Newton* PSDs. Note that these values do not correspond directly to the underlying PSD model shape parameters due to the presence of red noise leak. Errors on β_{obs} correspond to a change in χ^2 of $\Delta\chi^2 = 2.71$.

TABLE 4
CROSS CORRELATION FUNCTION RESULTS

Time Scale	Band 1	Band 2	ICF r_0	ICF τ	DCF r_0	DCF τ	F_{sims}
Short (Rev. 371)	S	M	0.98	+0.6±0.3 ks	0.98	0 ks	59/200
	S	H	0.92	+3.0±0.8 ks	0.90	+2.4 ks	17/200
	M	H	0.95	+1.8±0.6 ks	0.94	+1.2 ks	0/200
Short (Rev. 372)	S	M	0.97	+0.6±0.5 ks	0.96	0 ks	11/200
	S	H	0.88	+0.6±0.5 ks	0.87	0 ks	6/200
	M	H	0.96	+0.6±0.4 ks	0.96	0 ks	1/200
Medium	H1	H2	0.95	0±0.03 d	0.95	0 d	9/200
	H1	H3	0.90	0±0.03 d	0.90	0 d	0/200
	H1	H4	0.70	0±1.7 d	0.70	0 d	33/200
	H2	H3	0.90	0±0.05 d	0.90	0 d	0/200
	H2	H4	0.70	0±2.2 d	0.70	0 d	26/200
	H3	H4	0.73	0±1.9 d	0.73	0 d	77/200
Long	H1	H2	0.93	0±0 d	0.93	0 d	0/200
	H1	H3	0.94	0±0 d	0.94	0 d	0/200
	H1	H4	0.80	0±0 d	0.80	0 d	0/200
	H2	H3	0.95	0±0 d	0.95	0 d	0/200
	H2	H4	0.83	0±0 d	0.83	0 d	0/200
	H3	H4	0.84	0±0 d	0.84	0 d	0/200

Note. — Lags are defined such that a positive lag means band 2, the harder band, is delayed with respect to band 1, the softer band. The DCF bin size was the resolution of the light curve, e.g., 1200 s for the short-term data; the ICF resolution was one-half the DCF bin size. F_{sims} (Col. [8]) is the fraction of simulated light curves with r_0 greater than the observed value of r_0; this fraction is the confidence level at which the null hypothesis of the two light curves having unity coherence and a peak correlation coefficient of 1, with any lack of perfect correlation being due solely to Poisson noise, can be rejected.

TABLE 5
CROSS CORRELATION FUNCTION RESULTS, SR VS. SUMMED LIGHT CURVES

Time Scale	Light Curve 1	Light Curve 2	ICF r_0	ICF τ	DCF r_0	DCF τ	F_{sims} (peak lag)	F_{sims} (lag lower limit)
Short (Rev. 371)	S/M	S+M	0.89	+5.4±1.7 ks	0.87	0 ks	54/200	63/200
	S/H	S+H	0.90	+6.6±1.9 ks	0.89	+2.4 ks	18/200	40/200
	M/H	M+H	0.83	+7.8±4.1 ks	0.82	+1.2 ks	4/200	18/200
Short (Rev. 372)	S/M	S+M	0.69	+7.8±8.5 ks	0.69	+7.2 ks	52/200	105/200
	S/H	S+H	0.71	+5.4±6.0 ks	0.71	+6.0 ks	56/200	106/200
	M/H	M+H	0.66	+4.2±5.0 ks	0.65	+3.6 ks	55/200	105/200
Medium	H1/H2	H1+H2	0.48	−0.13± 4.9 d	0.44	0 d		
	H1/H3	H1+H3	0.55	−0.13± 4.9 d	0.49	0 d		
	H1/H4	H1+H4	0.48	+0.13± 5.3 d	0.40	+0.265 d		
	H2/H3	H2+H3	0.27	−0.13± 5.8 d	0.23	0 d		
	H2/H4	H2+H4	0.33	+0.13± 6.1 d	0.28	+0.265 d		
	H3/H4	H3+H4	0.32	+0.13± 6.1 d	0.31	+0.265 d		
Long	H1/H2	H1+H2	0.36	0±260 d	0.36	0 d		
	H1/H3	H1+H3	0.62	0±250 d	0.62	0 d		
	H1/H4	H1+H4	0.45	0±150 d	0.45	0 d		
	H2/H3	H2+H3	0.41	0±270 d	0.41	0 d		
	H2/H4	H2+H4	0.30	+2.1±400 d	0.29	0 d		
	H3/H4	H3+H4	0.11	+221±370 d	0.13	−123 d		

Note. — Lags are defined such that a positive lag means light curve 2, the summed light curve, is delayed with respect to light curve 1, the SR light curve. The DCF bin size was the resolution of the light curve, e.g., 1200 s for the short-term data; the ICF resolution was one-half the DCF bin size. F_{sims} (Col. [8] and [9]) show the fraction of simulated CCFs with a lag greater than the ICF peak lag and lag lower limit, respectively.
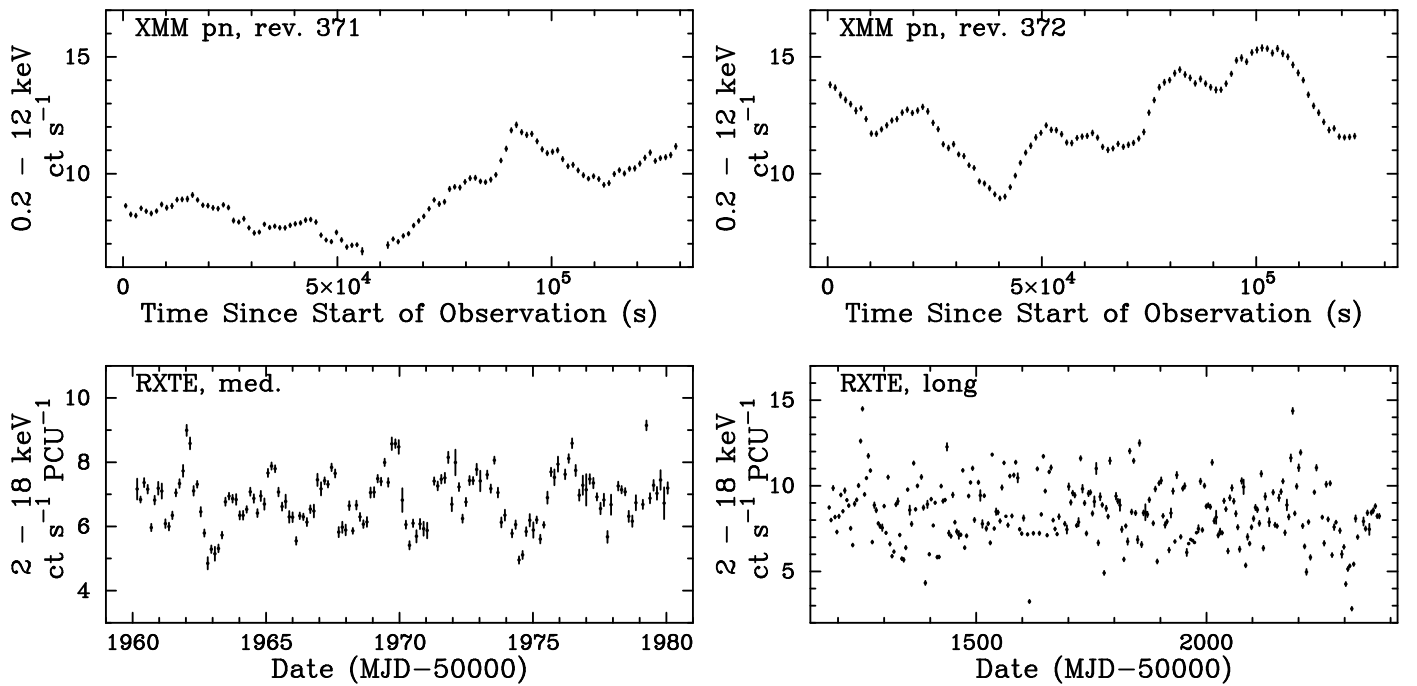
FIG. 1.— Total bandpass light curves for all time scales. Upper left: the revolution 371 *XMM-Newton* pn 0.2–12 keV light curve, which started on 2001 December 17 at 19:41 UTC. Upper right: the revolution 372 *XMM-Newton* pn 0.2–12 keV light curve, which started on 2001 December 19 at 19:33 UTC. Both pn light curves are binned to 1200 s. Note that the y-axes for both pn panels have the same scale. Lower left: 2–18 keV *RXTE* medium-term sampling light curve. Lower right: 2–18 keV *RXTE* long-term sampling light curve.
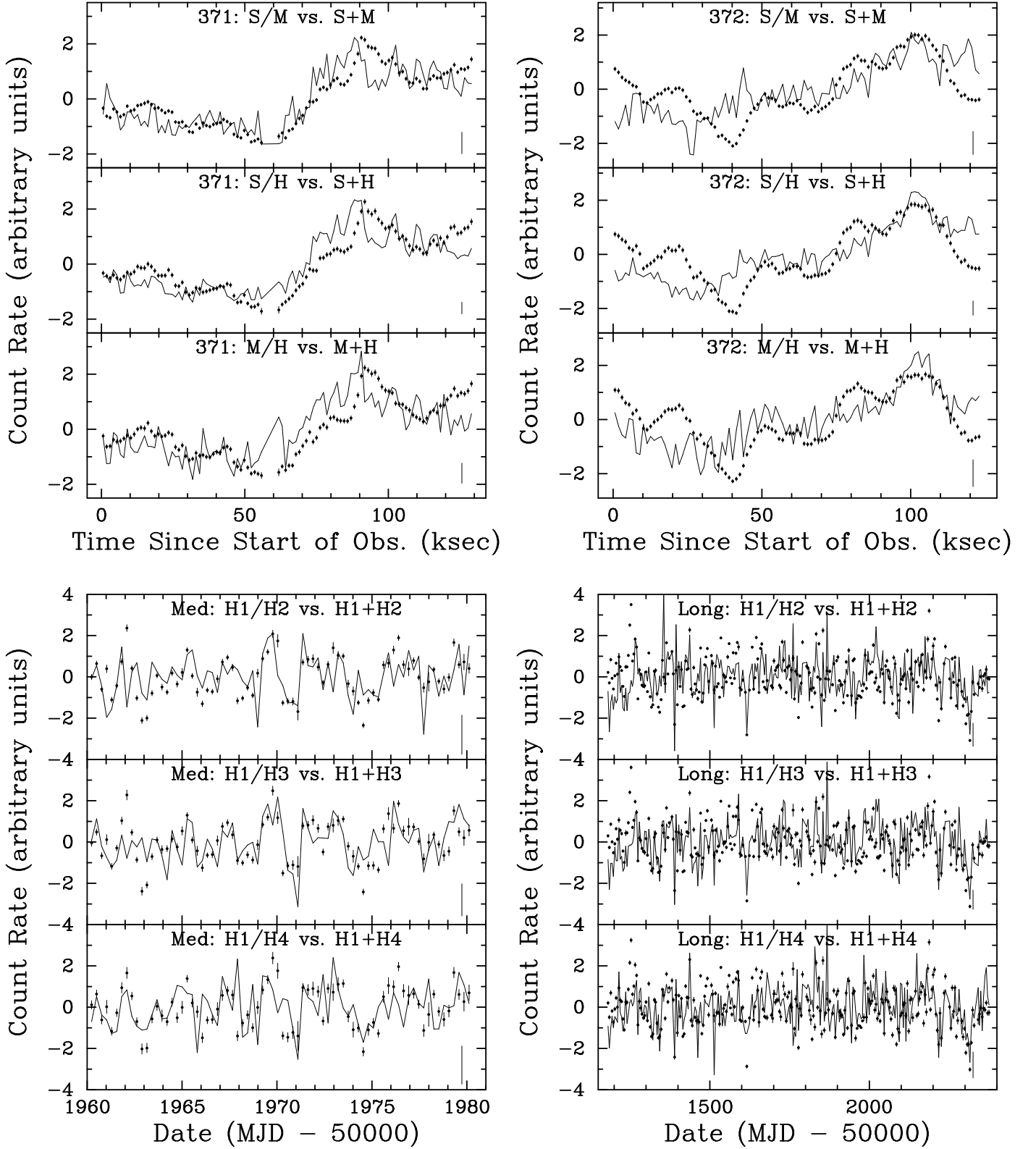
Fɪɢ. 2.— Softness ratio (SR) and summed band overplots. The solid lines denote SR light curves; the circles denote the summed band light curves. All light curves have been mean-subtracted and normalized by their standard deviation. For clarity, errors on the SR light curves are not plotted; the error bar in the lower right corner of each panel denotes the average two-sided error. There is a tentative tendency for the source to soften before it brightens on time scales of ∼ 5ksec.
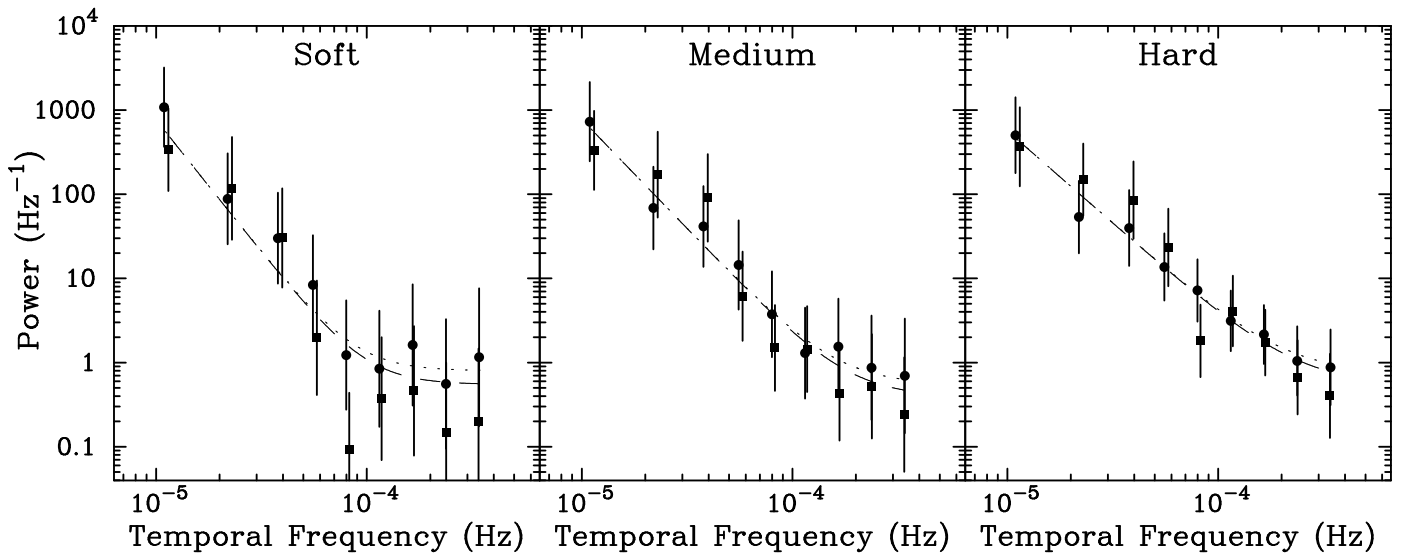
FIG. 3.— The best-fit PSD model shape for the soft, medium, and hard-bands are shown for rev. 371 (dotted line) and rev. 372 (dashed line). The effects of red-noise leak have been subtracted off. The symbols (circles for rev. 371 and squares for rev. 372) represent the difference between the average distorted model PSD and the observed PSD, plotted with respect to the underlying PSD model shape. The data are consistent with relatively softer bands having intrinsically steeper PSD slopes.
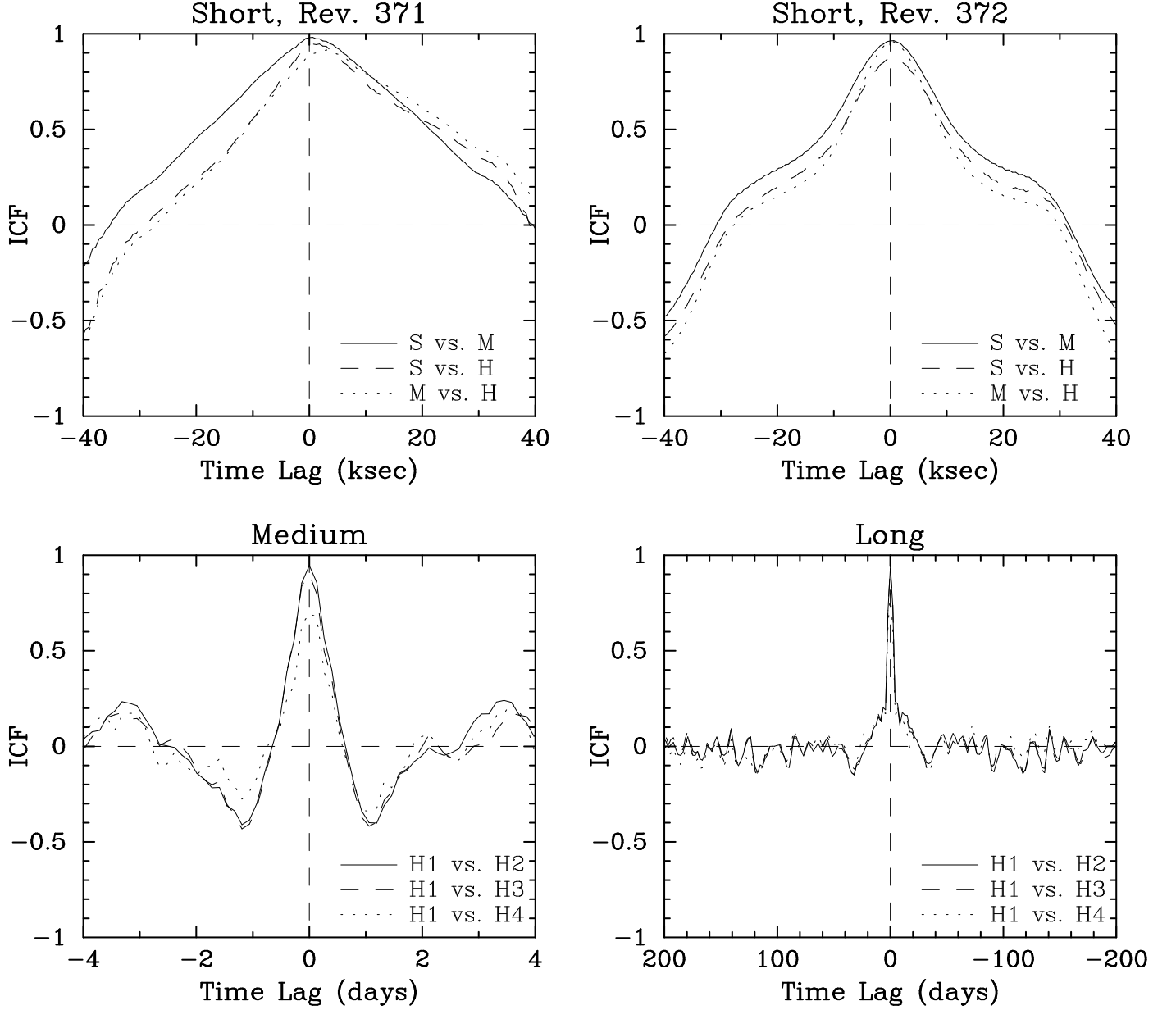
FIG. 4.— Cross-correlation functions are shown for all time scales. A positive lag indicates that hard photon variations lag those in the soft band. For clarity, the H2-H3, H3-H4 and H2-H4 medium- and long-term CCFs are not plotted.
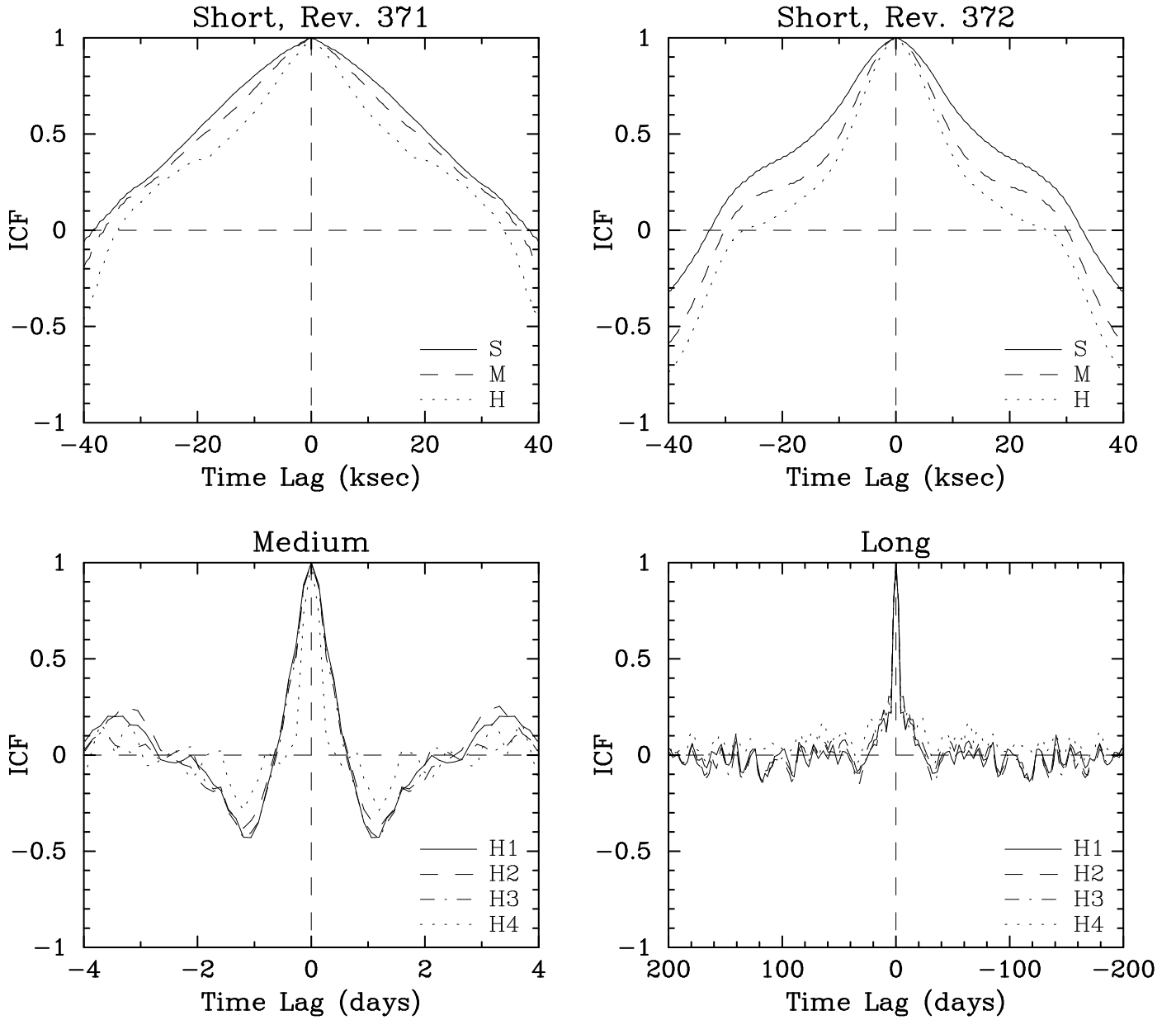
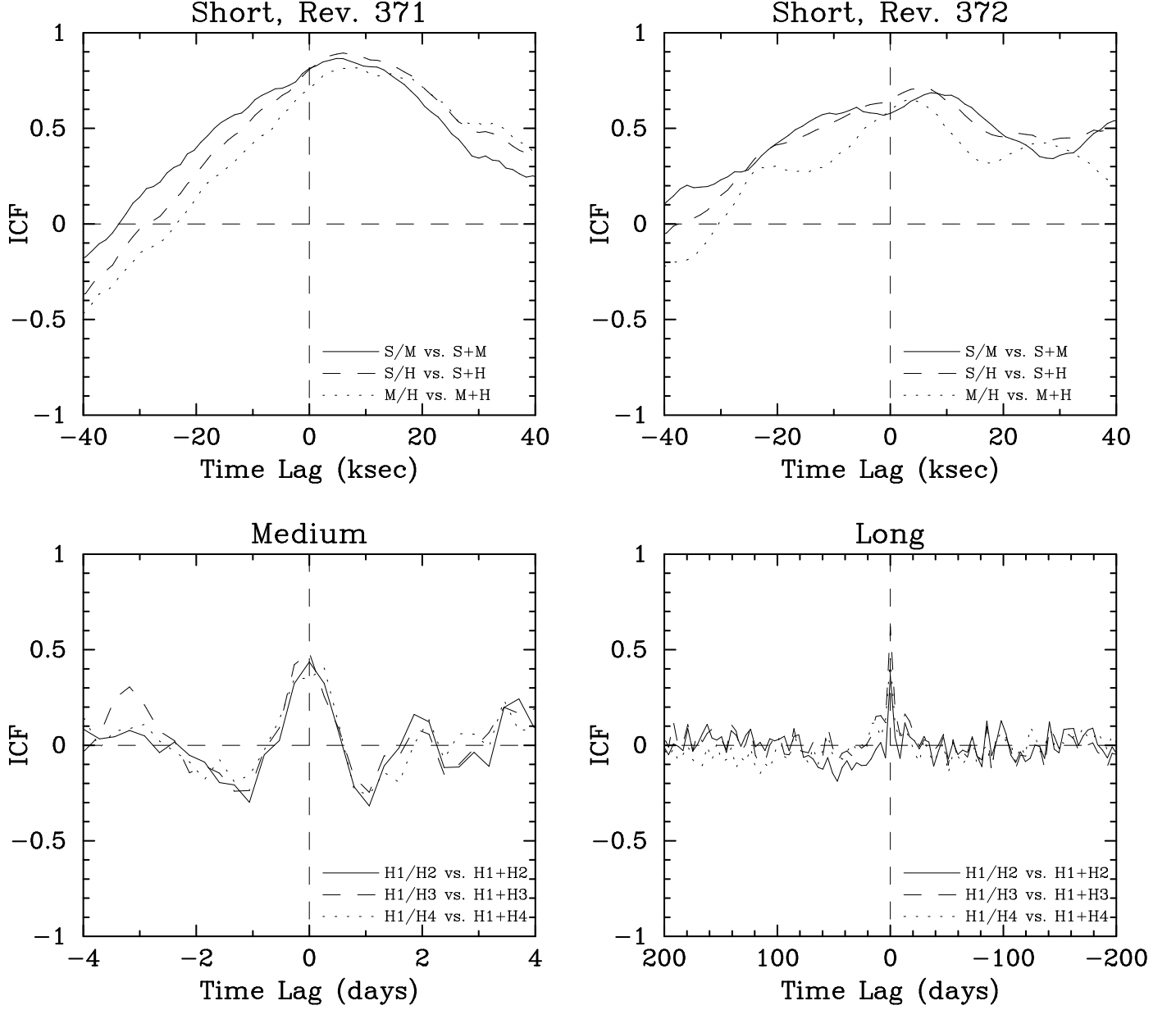FIG. 5.— Auto-correlation functions are shown for all time scales.

FIG. 6.— Cross-correlation functions for the softness ratio (SR) light curves against the summed band light curves, e.g., S/H versus (S + H). A positive lag indicates that variations in the summed band light curve lags those in the softness ratio light curve.
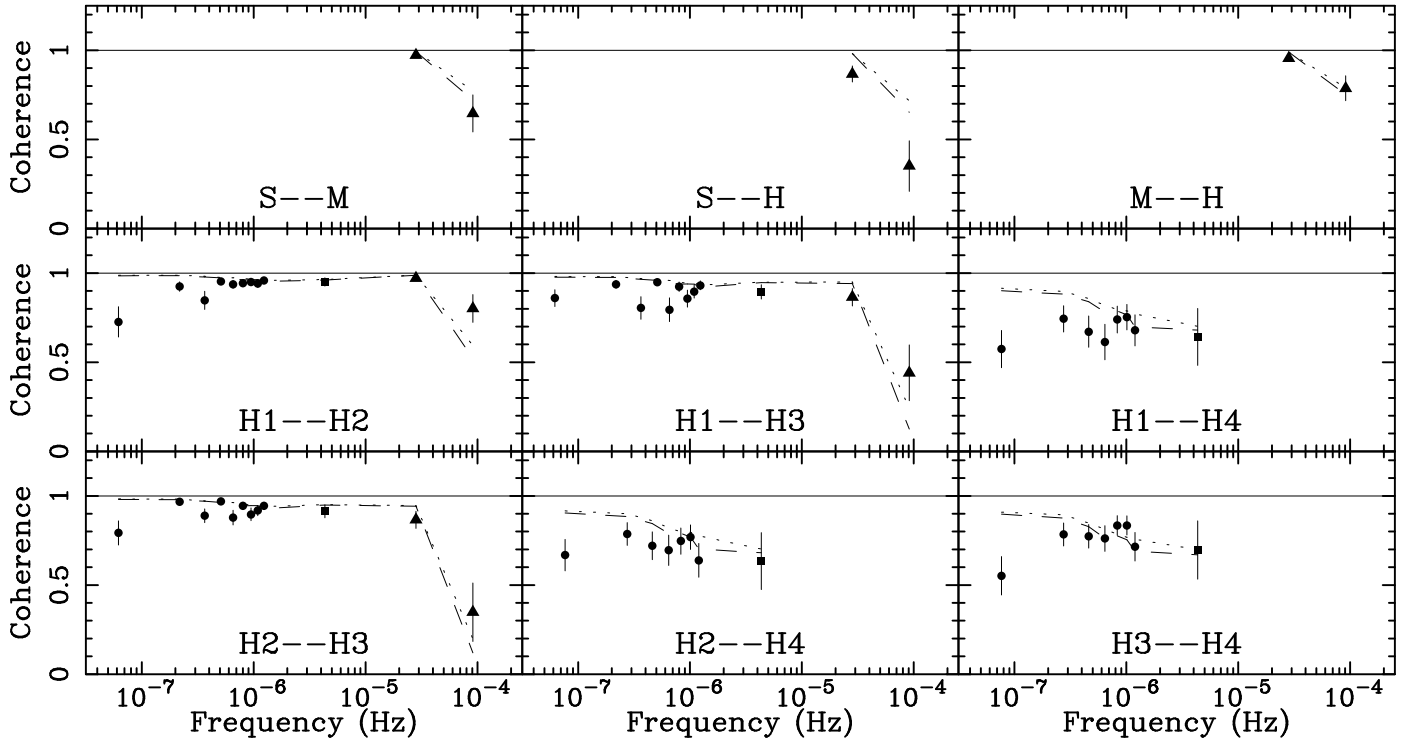
Fɪɢ. 7.— Coherence functions for all bandpass combinations are shown. Circles, squares, and triangles denote coherence measurements derived from the long, medium, and short time scale data, respectively. Unity coherence is indicated by the thin solid line. The dotted and dashed lines show, respectively, the 90% and 95% confidence limits for spurious lack of coherence due to Poisson noise. This was calculated independently for each time scale. For most temporal frequencies, the artificial drop in coherence is small, and especially at temporal frequencies below $\sim 10^{-6}$ Hz, the deviation of the intrinsic coherence from unity is greater than the artificial drop at greater than 95% confidence. An exception is the highest temporal frequency point in the short-term data (e.g., in the H2–H3 coherence plot), where the simulations show that the drop in coherence is likely an artifact of the Poisson noise. The intrinsic coherence has a tendency to decrease as the energy separation of the bands increases.
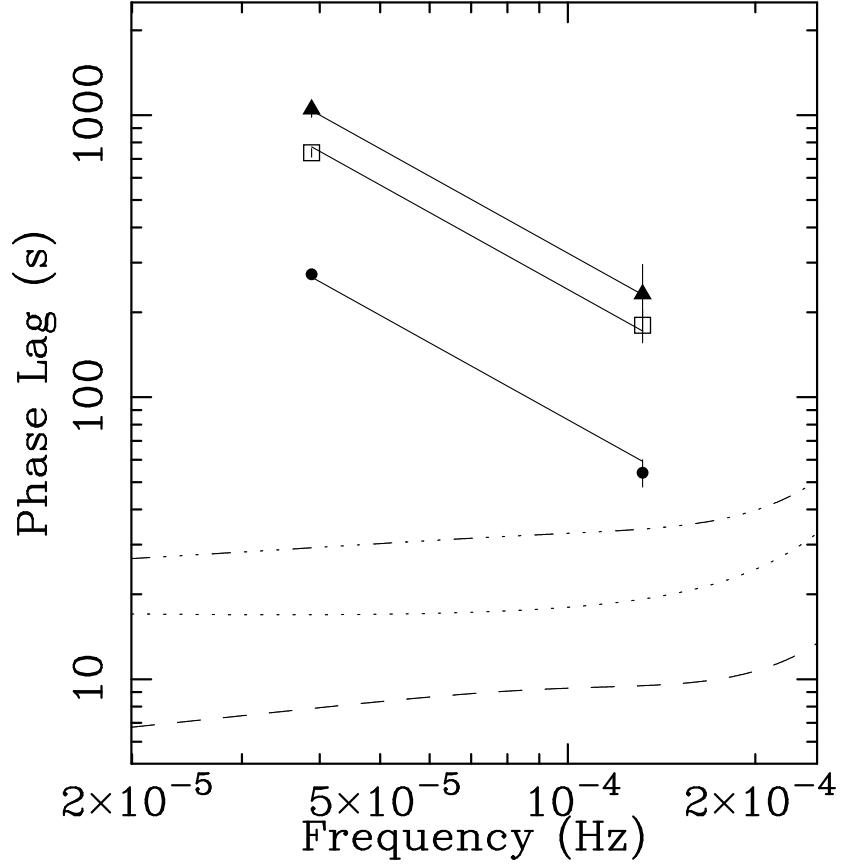
FIG. 8.— Phase lags versus temporal frequency derived from the short term data. Filled circles, open squares, and filled triangles show, respectively, the S–M, M–H, and S–H phase lags. Phase lags are consistent with increasing as the energy separation of the bands increases and as temporal frequency decreases. The solid lines denotes the relations $\phi(f) = 0.001 \ f^{-1.2}$ (for S–M), $\phi(f) = 0.003 \ f^{-1.2}$ (M–H), and $\phi(f) = 0.004 \ f^{-1.2}$ (S–H). The dotted, dashed, and dotted-dashed lines denote the phase lag sensitivity limits for the S–M, M–H, and S–H bands, respectively.